Tracing mercury from land to river: global sources, retention, and implications for sustainability

Dong Peng[1,2], Zeli Tan[3], Peipei Wu[4], Ruirong Chang[2], Shaojian Huang[2], Peng Zhang[2], Yujuan Wang[2], Zhengcheng Song[2], Yanxu Zhang[5*], Ting Lei[6], Maodian Liu[7], Beth A Middleton[8], Jianhua Gao[1], Junguo Liu[9], Guangchun Lei[6], Shu Tao[7,10]

[1]*School of Geography and Ocean Science, Ministry of Education Key Laboratory for Coast and Island Development, Nanjing University, Nanjing, China*

[2]*School of Atmospheric Sciences, Nanjing University, Nanjing, China*

[3]*Pacific Northwest National Laboratory, Richland, WA, USA*

[4]*Scripps Institution of Oceanography, University of California San Diego, La Jolla, CA, USA*

[5]*Department of Earth and Environmental Sciences, Tulane University, New Orleans, LA, USA*

[6]*School of Ecology and Nature Conservation, Beijing Forestry University, Beijing, China*

[7]*College of Urban and Environmental Sciences, Peking University, Beijing, China*

[8]*U.S. Geological Survey, Wetland and Aquatic Research Center, Lafayette, LA, USA*

[9]*Henan Provincial Key Laboratory of Hydrosphere and Watershed Water Security, North China University of Water Resources and Electric Power, Zhengzhou, China*

[10]*School of Environmental Science and Engineering, Southern University of Science and Technology, Shenzhen, China*

*Corresponding author: Yanxu Zhang (yzhang127@tulane.edu)

Peer review status:

This manuscript is currently under review by Environmental Science & Technology.

TOC

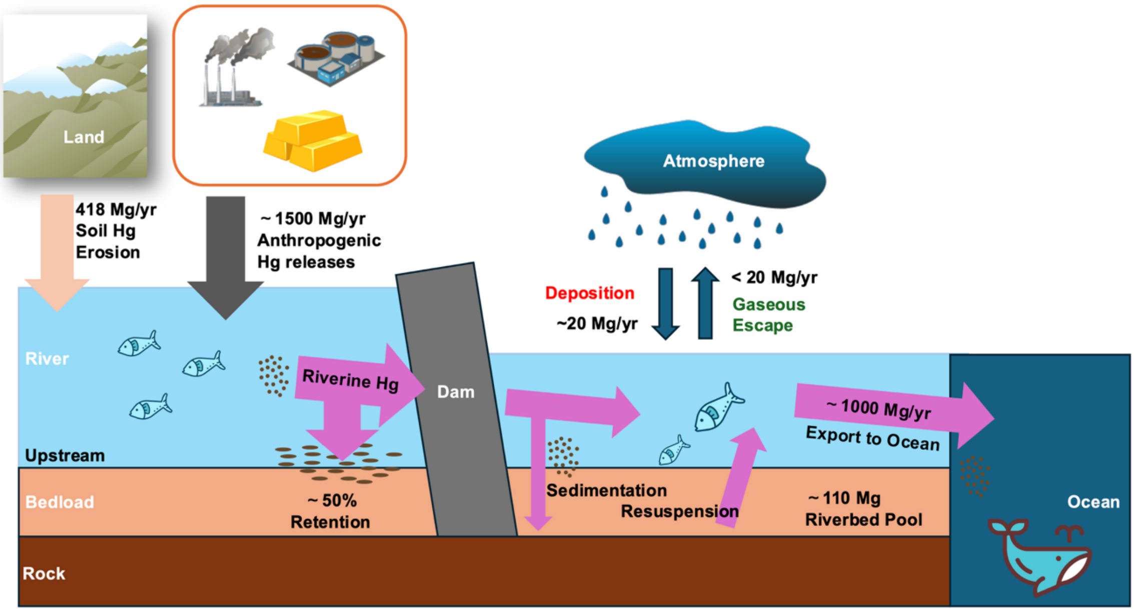

Keywords: mercury, riverine transport, anthropogenic mercury release, earth system model, water management, pollution governance

Abstract

Mercury (Hg) pollution in river systems is a global sustainability challenge. Yet the transport, transformation, and retention of Hg within global rivers remain poorly quantified, particularly in regions with sparse observations such as Southeast Asia and Africa, hindering effective pollution mitigation and reinforcing geographic inequities in scientific knowledge and environmental governance. Here, we present the first global, high-resolution simulation of riverine Hg dynamics using a process-based model that traces Hg from land-based sources through river networks to the ocean. Under a realistic scenario, we estimate that ~1,900 megagrams per year (Mg/yr) of Hg enters global rivers, including 1,500 Mg/yr from human-induced sources and 400 Mg/yr from soil erosion. Nearly half of this flux (~1,000 Mg/yr) is retained in reservoirs and dams, which act as major sinks. While such retention limits downstream delivery to the oceans, it also heightens in-reservoir Hg methylation risks. By bridging the gap between Hg releases and observed riverine exports, our framework offers a scalable tool for data-limited regions, promotes data access, and supports global freshwater and pollution-management strategies.

1. INTRODUCTION

Mercury (Hg) is one of the most toxic and persistent pollutants affecting river systems, posing serious threats to water quality, aquatic ecosystems, and human health worldwide [1-4]. As a key component of the global Hg cycle, rivers serve as critical conduits linking terrestrial Hg sources with oceanic reservoirs [1]. Extensive discharges of Hg-contaminated wastewater and industrial waste have elevated Hg concentrations in freshwater systems, leading to widespread bioaccumulation in aquatic organisms and increasing exposure risks for human populations [5-7]. These impacts undermine the capacity of rivers to provide clean water and safe food, particularly in communities reliant on freshwater fisheries [8]. To address this problem, regulatory measures such as the U.S. Clean Water Act and national fish consumption advisories have been introduced to mitigate riverine Hg pollution and its impacts [9, 10]. At the international level, the Minamata Convention on Mercury (refer to as Minamata Convention) seeks to reduce anthropogenic Hg emissions and release globally. Despite decades of localized monitoring efforts [11, 12], our understanding of the global-scale sources, transport pathways, and retention processes of riverine Hg remains fragmented. This limits the ability to design effective mitigation strategies and assess progress toward sustainability goals.

Riverine Hg originates from various natural and anthropogenic sources, including natural and legacy Hg releases by soil erosion, industrial wastewater (e.g., metal smelting and/or chlor-alkali production), and artisanal and small-scale gold mining (ASGM) [13]. At present, anthropogenic releases are the primary contributors to global riverine Hg [14]. However, there are relatively large uncertainties associated with the existing release inventories to rivers. For example, Kocman, et al. [14] estimated that approximately 1,000 Mg (300-1300 Mg) of anthropogenic Hg is discharged into global water systems annually, with contributions of 220 Mg from point sources, 40 Mg from the remobilization of contaminated systems, and 440 Mg from ASGM. In another study, Streets, et al. [15] estimated that the amount of global Hg released to land and water is reached up to 7,280 Mg by 2010 but noted the challenge in separating releases between land and water due to a lack of data. Anthropogenic Hg emissions and releases have shifted from developed regions to developing regions [5, 16], where ASGM and fuel combustion remain high even after the Minamata Convention [13]. These developing regions often have less stringent environmental regulations and limited Hg monitoring in river systems, potentially increasing the risk of Hg exposure for both humans and wildlife. Consequently, a process-based modeling approach can help address these gaps and promote more equitable Hg governance.

Riverine Hg primarily exists in the form of particulate Hg within suspended particulate matter (SPM) in rivers [17, 18]. Thus, the riverine Hg is largely influenced by sediment flux [1, 2]. At the global scale, the majority of riverine Hg discharge is in the particulate phase [1, 19]. Natural processes, especially soil erosion, are important contributors to riverine Hg concentrations and fluxes [20], and they influence Hg concentrations in SPM in rivers [2, 21]. Human activities, particularly those related to water management practices (e.g., the construction of reservoirs and dams worldwide), profoundly impact the processes governing riverine Hg transport in contemporary times. Reservoirs have substantial efficacy in trapping SPM [22-24], leading to the potential accumulation of Hg-laden sediments behind dams. For example, the Three Gorges Dam in China has resulted in the settling of 100-200 Mg of riverine Hg in bedload [2] and has reduced the downstream flux of riverine Hg by more than 70% [20]. However, the overall impact of reservoirs and dams on river Hg transport at a global scale remains poorly understood.

In this study, we develop a process-based global Hg model, to simulate the contemporary transport and fate of Hg in global river systems. While previous work [25] quantified long-term anthropogenic perturbations on coastal Hg export via pre-industrial baselines, it lacked dynamic simulations of contemporary anthropogenic Hg processes within land-river systems. This study shifts the focus to modern temporal scales to investigate active biogeochemical mechanisms. By explicitly coupling a water management [26] with dynamic in-stream sediment routing, we resolve certain components of the process including contemporary terrestrial erosion, dam trapping, in-channel sedimentation and resuspension. Note the term of “trapping” hereafter refers to the retention of materials within reservoirs or dams as simulated by the water management module. This structural advancement explicitly partitions transient riverbed sinks from permanent reservoir retention. Furthermore, using scenario-based perturbations of anthropogenic Hg releases, we systematically quantify active Hg inventories and assess how localized inputs propagate through global watershed.

We hypothesize that (1) river routing and water infrastructure reshape the magnitude and composition of Hg delivered to oceans, (2) human-induced terrestrial Hg releases dominate present-day riverine Hg transport, and (3) reservoir trapping produces geographically uneven Hg retention, altering coastal accumulation patterns. The study aims to (1) model present-day riverine Hg transport and export fluxes, including human-induced releases and the effects of reservoirs and dams, (2) quantify key processes controlling Hg transport to downstream sinks, and (3) estimate global Hg accumulation within reservoirs. Here, riverine transport flux refers to Hg fluxes conveyed within river channels, whereas riverine export flux denotes the Hg flux ultimately delivered by rivers to the oceans. By resolving inland rivers and reservoir retention globally, our framework provides a scalable tool for data-limited regions, informs more equitable Hg pollution and exposure management, and enables assessment of freshwater food safety, particularly in low-income regions. In doing so, this work can inform efforts to improve freshwater sustainability and access, particularly by clarifying how contaminant transport affects riverine water quality.

2. METHODS

2.1 Model platform

In this study, we introduce the MOdel for Scale Adaptive River Transport for Mercury under WateR Management (MOSART-Hg-WM) to simulate Hg cycling in land-river systems. This framework builds upon our previous MOSART-Hg model [25] by integrating a water management module to represent reservoir dynamics [26, 27]. MOSART-Hg-WM is implemented within the Community Earth System Model version 2.1.3 (CESM2.1.3). It incorporates advanced physical modules originally developed for the Energy Exascale Earth System Model (E3SM), specifically coupling the core Hg cycling processes with modules for sediment transport [28], dam trapping [26], and land erosion [29, 30].

The physical hydro-sedimentological performance of this model architecture, including soil erosion, runoff, and dam trapping, has been thoroughly validated in prior studies [26, 28-32]. In this paper, we use the same present-day land-river Hg framework applied in Peng et al. (2025) [25], including the validated water management module for dam trapping, and refer to this configuration as MOSART-Hg-WM to distinguish it from the pre-industrial configuration without modern dam regulation (MOSART-Hg). The underlying Hg biogeochemical processes remain unchanged from the previously established MOSART-Hg framework. The water management module was originally developed within E3SM [26], and is implemented here in CESM-MOSART-Hg to simulate Hg trapping by dams. Regarding fixed riverine boundary conditions, the model incorporates soil erosion as the primary input vector for natural and legacy Hg, while explicitly accounting for contemporary anthropogenic releases. Here, legacy Hg refers to the elevation of soil Hg concentrations relative to the ~1850 baseline (natural background), arising from the cumulative accumulation of Hg via atmospheric deposition and other input pathways. Erosional Hg fluxes are calculated as the product of the eroded sediment flux and the corresponding soil or sediment Hg concentration. The detailed mechanistic processes governing this mobilization are described in previous work [25]. Furthermore, while atmospheric Hg can enter rivers directly via precipitation, this model focuses exclusively on indirect loading via watershed runoff and soil erosion. Direct atmospheric deposition to the water surface is considered negligible in this framework due to the minimal surface area of the river network relative to the total catchment area [33].

Since the water management module has been integrated, the model now accounts for global reservoir construction, determining reservoir trapping efficiency [22, 26, 27]. The model facilitates the determination of trapping efficiency by leveraging input datasets of global dams through the calculation method outlined by Vörösmarty, et al. [22]. Consequently, the sediment trapping processes can be effectively ascertained. This methodology finds broad application in hydrology and biogeochemical models, exemplified by its utilization in models such as the Global Nutrient Export from Watersheds 2 (NEWS 2) [34]. Data on global reservoirs are sourced from the Global Reservoir and Dam (GRanD) database [35], initialized on a grid basis by Zhou, et al. [26], and originally implemented in E3SM simulations. This dataset encompasses dam locations, reservoir capacities, and major functions for over 4,200 dams worldwide. The trapping efficiency is calculated as follows [22, 28]:

$$e_{trap} = 1 - \frac{0.05}{\Delta t_{local}^{0.05}} \quad (1)$$

where $\Delta t_{local}^{0.05}$ is the increase of local water residence time due to the reservoir [years], estimated as the effective reservoir storage capacity divided by the mean annual inflow from the reservoir upstream.

The deposition of particulate Hg to the riverbed is governed by the MOSART sediment routing scheme, occurring dynamically when local flow velocities decrease in low-gradient reaches and the suspended particulate load exceeds the flow transport capacity. Because the model operates at 0.5° or 1° spatial resolution, rivers and reservoirs are represented as sub-grid parameters rather than explicitly resolved spatial polygons. Consequently, direct surface area ratios between rivers and reservoirs are not defined. Reservoir trapping of Hg is instead mathematically parameterized (Eq. 1), utilizing sub-grid flow dynamics and water residence times to calculate retention efficiency.

The simulations span the period 1995-2004, with the initial five years used to establish the steady state of the simulated river systems (i.e., spin-up), and the subsequent five years are considered for analysis. The spatial resolution matches that of previous studies, with the Community Land Model 5.0 for Mercury (CLM5-Hg) [25], and MOSART-Hg-WM running at resolutions of 0.9°×1.25° and 0.5°×0.5°, respectively. The former has been extensively evaluated in simulating erosional Hg dynamics [25]. We include global soil Hg datasets from Wang et al. [36] and Liu et al. [37] to represent its uncertainties (Table 1). Furthermore, the model explicitly simulates the in-stream sedimentation of Hg.

Climate forcing data, obtained from the Global Soil Wetness Project Phase 3 (GSWP3) dataset [38], spans the same temporal range as previous studies (1995-2014) with a six-hour time resolution. Climate forcing dataset parameters include Precipitation (mm H_2O/sec), Incoming Solar Radiation (W/m^2), Temperature (K), Pressure (Pa), Winds (m/s), Humidity (kg/kg), and Downward Longwave Radiation (W/m^2). The datasets of the land use and land cover following the datasets of Land Use Harmonization 2 (LUH2, luh.umd.edu/data.shtml) at present-day [39], and other surface datasets following the setting of CLM5 [40]. By incorporating a range of land unit datasets, our simulations capture the impacts of land use and land cover changes, including deforestation, agriculture, and urbanization. The specific simulations conducted in this study are summarized in Table 1.

2.2 Inventory of Anthropogenic Hg release for rivers

Existing global inventories report total Hg releases without specifying the fractions partitioned between land and water [15], leaving source-specific aquatic release fractions highly uncertain. For example, the Kocman inventory [14] estimates a lower-bound anthropogenic Hg release of ~1,000 Mg/yr to global rivers; however, directly applying this value to drive MOSART-Hg-WM in preliminary simulations yields unrealistically low Hg export to the oceans, indicating a mismatch between inventory assumptions and observed riverine fluxes. To address this limitation, we extend previous global riverine Hg assessments focused on estuaries and coastal fluxes (e.g., Liu, et al. [1,] Amos, et al. [19]) to explicitly represent inland river channels and reservoirs/dams. Model performance is evaluated against riverine Hg observations reported in the literature. Building on this framework, we construct a global, grid-resolved inventory of Hg releases to surface waters by adopting the ASGM fraction of total anthropogenic Hg releases as defined in Kocman et al. [14]. Unlike prior source-based approaches [14, 41], our inventory is constrained from an observational perspective, enabling a more realistic representation of Hg inputs to rivers, particularly in the absence of comprehensive statistics and reports from these sources [15].

To constrain sector-specific release fractions and reduce these uncertainties, we developed an inverse estimation framework. First, to define the spatial distribution of aquatic Hg releases, we used atmospheric Hg emission inventories [e.g., Arctic Monitoring and Assessment Programme (AMAP) inventory [42], and Streets inventory [43]] as spatial proxies for anthropogenic sources to rivers. This approach is justified by evidence that major anthropogenic Hg emissions to the atmosphere, land, and water broadly share similar spatial patterns [15]. To minimize inconsistencies where atmospheric and aquatic release pathways diverge, we limited the analysis to three core AMAP sectors including industrial activities (INDS), energy production (POWERGEN), and artisanal and small-scale gold mining (ASGM). Sectors with weak or poorly aligned links to aquatic releases, such as the intentional-use waste (INTWASTE) category in the AMAP inventory, were excluded.

Second, to quantify the specific release coefficients for these selected sectors, we applied a top-down constraint based on the global amount of Hg exported to oceans, approximately 1,000 Mg/yr as derived from the river mouth monitoring data [1]. The Hg releases from human-induced sources to rivers are categorized as direct and indirect releases (i.e. the short-term legacy Hg release). Direct release involves Hg discharged into rivers via such as urban sewage pipe networks, while indirect release entails Hg initially deposited in soil, mobilized by erosional processes, and transported to rivers over a period of one year. The sediment yield serves as a crucial parameter for determining indirect release. In this study, the sediment yield dataset represents the mean sediment yield in 2010, estimated under the ***No Release scenario*** (Table 1). The simulation of sediment yield is decoupled from Hg cycling, so the sediment yield remains the same across all scenarios.

Given validated runoff and sediment simulations as boundary conditions, we iteratively calibrated the sector-specific release coefficients [i.e., the *Coef* terms in *Eqs. (2)-(7)*] to match this global ocean Hg export target. Within this constrained source-sink framework [25], the derived coefficients for ASGM of direct releases are strictly higher than those for industrial sources, reflecting its direct aquatic discharge pathways, while INDS and POWERGEN share identical coefficients under the same simulation scenarios (Table 2). The grid-based anthropogenic Hg releases to rivers are calculated by the following equations:

$$EI_{ASGM}^{THg} = AMAP_{ASGM}^{THg} \times Sed_{yld} \times Coef_{ASGM}^{I} \qquad (2)$$

$$EI_{INDS}^{THg} = AMAP_{INDS}^{THg} \times Sed_{yld} \times Coef_{INDS}^{I} \qquad (3)$$

$$EI_{POWERGEN}^{THg} = AMAP_{POWERGEN}^{THg} \times Sed_{yld} \times Coef_{POWERGEN}^{I} \qquad (4)$$

where $EI_{ASGM}^{THg}, EI_{INDS}^{THg}, EI_{POWERGEN}^{THg}$ represent the indirect release by ASGM, industrial, or power-generation sectors, respectively (unit: g/km^2/yr); $AMAP_{ASGM}^{THg}$, $AMAP_{INDS}^{THg}, AMAP_{POWERGEN}^{THg}$ represent the spatial distribution of release from different sectors (unit: g/km^2/yr); Sed_{yld} represents the sediment yield (unit: kg/m^2/s); and $Coef_{ASGM}^{I}$, $Coef_{INDS}^{I}, Coef_{POWERGEN}^{I}$ represent the coefficient of Hg release associated with erosion of different sectors (unit: m^{2}s/kg). The settings of the Coefs are given in Table 2.

$$ED_{ASGM}^{THg} = AMAP_{ASGM}^{THg} \times Coef_{ASGM}^{D} \qquad (5)$$

$$ED_{INDS}^{THg} = AMAP_{INDS}^{THg} \times Coef_{INDS}^{D} \qquad (6)$$

$$ED_{POWERGEN}^{THg} = AMAP_{POWERGEN}^{THg} \times Coef_{POWERGEN}^{ID} \qquad (7)$$

where $ED_{ASGM}^{THg}, ED_{INDS}^{THg}, ED_{POWERGEN}^{THg}$ represent the direct release for varied sectors (unit: g/km^2/yr); $AMAP_{ASGM}^{THg}$, $AMAP_{INDS}^{THg}, AMAP_{POWERGEN}^{THg}$ represent the spatial distribution of release (unit: g/km^2/yr); and $Coef_{ASGM}^{D}$, $Coef_{INDS}^{D}, Coef_{POWERGEN}^{D}$ represent the coefficient of direct Hg release by sectors (dimensionless).

$$E_{total}^{THg} = EI_{ASGM}^{THg} + EI_{INDS}^{THg} + EI_{POWERGEN}^{THg} + ED_{ASGM}^{THg} + ED_{INDS}^{THg} + ED_{POWERGEN}^{THg} \qquad (8)$$

where E_{total}^{THg} represents the total anthropogenic Hg release to rivers, which is eventually used to drive the MOSART-Hg-WM model. The coefficients in equations (2) to (7) are adjustable to fit the requirements of various scenarios (Table 2).

Following a series of preliminary simulations, we find that a total anthropogenic Hg release of 1,100–2,000 Mg/yr provides the most realistic range for global riverine Hg simulations (Table 2, 3). This corresponds to an estimated global riverine Hg export to the oceans of 777–1,275 Mg/yr, which is within ±25% of the previous estimate of ~1,000 Mg/yr reported by Liu et al. [1]. Our estimates assumed that ASGM accounts for 30–48% of total anthropogenic Hg inputs to rivers (Table 2). This range is consistent with the Kocman inventory assumption of ~40%[14], and lower than the Global Mercury Assessment 2018 (GMA2018) [16], which assumes ~ 50% contribution from ASGM. In contrast, Horowitz et al. [41] estimated a substantially higher ASGM contribution to water than those estimations in global scale, with approximately 80% of total

Hg releases to water attributed to ASGM. Such high ASGM contributions would be particularly pronounced in regions with intensive ASGM activity, such as the Amazon, where simulations show strong sensitivity to the assumed ASGM emissions (refer to *Section 3.5*). Model sensitivity tests further show that relatively small shifts in ASGM fraction can induce disproportionate changes in riverine Hg export; for example, a 12% increase in ASGM contribution is related to a 32% increase in Hg fluxes in the Amazon (refer to *Section 3.5*).

In this study, anthropogenic Hg releases to rivers have been modeled in several scenarios to encompass different release situations for the present-day (Table 2). We consider five scenarios to analyze the uncertainties of anthropogenic Hg releases from industrial and ASGM sources to the rivers at present-day (*Inventory Experiment*): (1) *Low Release* (1,100 Mg/yr), (2) *Moderate Release* (1,500 Mg/yr) (similar level with *Baseline Scenario*), (3) *High Industrial Release* (2,000 Mg/yr, ASGM contribute 600 Mg/yr), (4) *High ASGM Release* (2,000 Mg/yr, ASGM contribute 850 Mg/yr), (5) *No Release* (0 Mg/yr). Other parameters in the model simulations, such as the number of dams, remain unchanged to ensure that human-induced Hg release is the sole variable in the control experiments.

The *Low Release scenario* represents the unique period during the COVID-19 pandemic when industrial and ASGM releases are significantly reduced due to lockdown measures [44, 45]. The around –40% reduction in indirect ASGM releases relative to *Moderate Release* scenario reflects decreased human activities, such as agricultural activity during lockdown periods [46] (Table 2). In contrast, direct ASGM emissions are assumed to remain unchanged across scenarios, as overall production is considered stable during lockdowns, with increased illegal mining activity offsetting partial disruptions to formal ASGM operations [45]. The *Moderate Release scenario* represents a more realistic post-Minamata Convention condition with reduced anthropogenic Hg releases compared to the high-releases scenarios [1]. However, it still retains relatively higher industrial (~+60%) and indirect ASGM releases (~+60%) than lockdown-period levels, reflecting the recovery of human activities following the pandemic.

The *High Industrial Release scenario* represents conditions around the year 2000, characterized by elevated industrial Hg releases (~55% higher than the Moderate Release scenario), reflecting less effective environmental management and weaker regulatory controls [19]. The *High ASGM Release scenario* represents an alternative pathway for the same period, in which industrial releases are moderately increased (~30%) while ASGM activity is further enhanced, leading to a larger overall ASGM contribution (~40%). The *High Industrial Release* and *High ASGM Release scenarios* share the same total global Hg release but differ in the relative contributions from industrial sources and ASGM. This design isolates the effects of sectoral composition on riverine Hg dynamics under a constant total Hg loading (refer to *Section 3.5*). The *No Release scenario* is an idealized case in which only erosional Hg inputs are considered under present-day conditions. Together, these scenarios allow assessment of the sensitivity of riverine Hg dynamics to variations in sector-specific anthropogenic inputs.

To better reproduce observed riverine Hg exports, we adopt the AMAP spatial distribution under the *Moderate Release scenario*, except in North America where the Streets inventory is applied (also under the *Moderate Release scenario*), as the AMAP pattern leads to overestimated Hg export in this region. This hybrid configuration is hereafter referred to as the *Revised AMAP Release scenario* and is used as the Hg input dataset for the ***Baseline scenario*** in this study. A comparison of the uncertainty associated with these alternative spatial distributions is provided in Fig. S3. The primary experiment (***Baseline scenario***) therefore employs total Hg release inputs of ~1,500 Mg/yr with this combined AMAP-Streets spatial pattern (Table 1, Table 2). This experiment facilitates a realistic representation of the present-day scenario by closely aligning with observational records.

2.3 Experimental Design

In this study, due to the absence of key parameters such as carbon concentration and plankton distribution in the MOSART model, we assume that Hg in rivers primarily exists in the particulate phase, partially following sedimentation and sediment resuspension processes to simplify the model (refer to Text S1). Despite these assumptions, accurately representing Hg fluxes from land to ocean remains our primary goal. A series of grouped experiments are devised to evaluate sensitivities and uncertainties stemming from different processes: *Reservoir* (with or without reservoir), *Inventory* (spatial distribution following AMAP or Streets Atmosphere inventories), *Soil Hg* (soil Hg concentrations following Wang or Liu dataset), and *Deposition* (with atmospheric deposition or not) (Table 1). Specifically, as for the *Reservoir Experiment*, we conduct paired sensitivity experiments to evaluate the role of reservoirs and dams in Hg sequestration and downstream release. Those sensitivity experiments include comparisons of: *No Human-induced Hg Release with/without Reservoir* (*NHHR w/wt R*)*, Baseline Human-induced Hg Releases with/without Reservoir* (*BHHR w/wt R*) (Table 1).

In the *Soil Hg* and *Deposition Experiments*, we conduct paired experiments to test the sensitivities of soil Hg datasets and atmospheric deposition, respectively (Table 1). To address the uncertainties stemming from soil Hg, we conduct the *Soil Hg Experiments* involving various soil Hg concentration datasets (referred to as the Liu dataset by Liu, et al. [37] and Wang dataset by Wang, et al. [36]). The Wang dataset's simulation outputs closely match previous estimation [1] (refer to *Uncertainty analysis*), so we apply it as the primary dataset for baseline simulations. We tested the effect of dynamic soil Hg concentrations driven by contemporary atmospheric deposition inputs and erosion-driven losses (refer to *Deposition Experiments*, Table 1).

The *Deposition Experiment* is designed to isolate the short-term response of soil Hg to contemporary atmospheric deposition. In the dynamic configuration (*Deposition*), soil Hg concentrations are allowed to evolve during the 10-year simulation, increasing through atmospheric deposition inputs and decreasing via erosion. In the *Without Deposition* configuration, soil Hg concentrations are held constant and do not respond to atmospheric inputs over the simulation period. Both configurations start from the same prescribed soil Hg fields, which incorporate the steady-state natural Hg cycle together with the cumulative legacy of anthropogenic emissions relative to the pre-industrial baseline. Therefore, the long-term accumulated Hg in soils is identical in both experiments. Therefore, long-term accumulated Hg in soil is identical in both experiments. The difference between the two experiments thus reflects only the short-term soil Hg adjustment driven by present-day deposition during the 10-year simulation window.

Table 1 Experimental Design.

Experiment ID	Experiment condition	Soil Hg concentration dataset	Anthropogenic Hg release (Mg/yr)	Release scenario*	Soil Hg dynamic	Atmospheric Hg deposition	Water Management (Reservoir)	Spatial distribution of release	LULCC dynamics
Baseline		Wang (dataset)	~1500	*Revised AMAP*	Constant	No	Yes	AMAP2015	*LUH2*
Anthropogenic release uncertainty			0	*No*					
			1100	*Low*					
			1500	*Moderate*					
			2000	*High ASGM*					
			2000	*High Industrial*					
Reservoir	No Release without Reservoir (R)		0	*No*			No		
	No Release with R						Yes		
	Baseline without R		~1500	*Revised AMAP*			No		
	Baseline with R						Yes		
Inventory	AMAP		1500	*Moderate*			Yes	AMAP 2015	
	Streets							Streets	
Soil Hg	Wang	Wang						AMAP 2015	
	Liu	Liu							
Deposition	Deposition	Wang			Dynamic	Yes			
	Without Deposition				Constant	No			

***Caption**: * the details of the release scenarios are given in Table 2. LULCC represents Land Use and Land Cover Change, Wang represents the soil Hg dataset from Wang, et al. [36], Liu represents the soil Hg concentration from Liu, et al. [37], AMAP2015 represents the inventory by Steenhuisen and Wilson [42,] Steenhuisen and Wilson [47], Streets represents the inventory of Streets, et al. [43]. LUH2 represents the land use and land cover datasets of Land Use Harmonization 2.*

Table 2 The scenarios of industrial releases and artisanal and small-scale gold mining (ASGM) **releases to rivers.**

Scenarios	**Anthropogenic Hg budget (Mg/yr)**	**Changes (Mg/yr)**	**Indirect release [Mg/yr (Coef.)]**			**Direct release [Mg/yr (Coef.)]**			**% from ASGM**
			ASGM	**Industrial**		**ASGM**	**Industrial**		
				INDS	POWERGEN		INDS	POWERGEN	
No Release	0	= 0	0 (0)	0 (0)	0 (0)	0 (0)	0 (0)	0 (0)	0
Low Release	1100	= No Release + 1100	147 (0.6*1e-6)	72(0.82*1e-7)	5 (0.82*1e-7)	378 (0.35)	460 (0.08)	36 (0.08)	48%
Moderate Release	1500	= Low Release + 400	232 (0.95*1e-6)	84 (0.95*1e-7)	6 (0.95*1e-7)	378 (0.35)	748 (0.165)	59 (0.165)	41%
Revised AMAP Release	~1500	≈ Moderate Release							
High Industrial Release	2000	= Moderate Release + 500	232 (0.95*1e-6)	343 (0.39*1e-6)	25 (0.39*1e-6)	378 (0.35)	949 (0.165)	74 (0.165)	30%
High ASGM Release	2000	= Moderate Release + 500	367 (1.5*1e-6)	132 (1.5*1e-7)	9 (1.5*1e-7)	475 (0.44)	949 (0.165)	74 (0.165)	42%

Caption: the Coef. refer to the coefficients in equations (2) to (7), the % of ASGM represents the percentage of anthropogenic Hg releases originated from ASGM.

Table 3 Fates of riverine mercury under different scenarios.

Scenarios	**Anthropogenic Hg releases (Mg/yr)**	**Inputs of riverine Hg (Mg/yr)**	**Outputs of riverine Hg (Mg/yr)**	**Increased release* (Mg/yr)**	**Increased outputs (Mg/yr)**	**Increased export/ increased releases (%)**	**Dam Trapping Rate (%)**
No	0	418	248	0	–	–	41%
Low	1100	1498	777	1100	529	48%	48%
Moderate	1500	2005	1007	400	230	58%	50%
High Industrial	2000	2532	1146	500	139	28%	55%
High ASGM	2000	2436	1275	500	268	54%	48%
Baseline	~1500	2032	1014	–	–	–	50%

**Caption**: * the increased Release as compared with the previous one, such as ‘moderate – low = 400’, ‘high -moderate=500’.

3 RESULTS AND DISCUSSIONS

3.1 The global riverine Hg sources and sinks

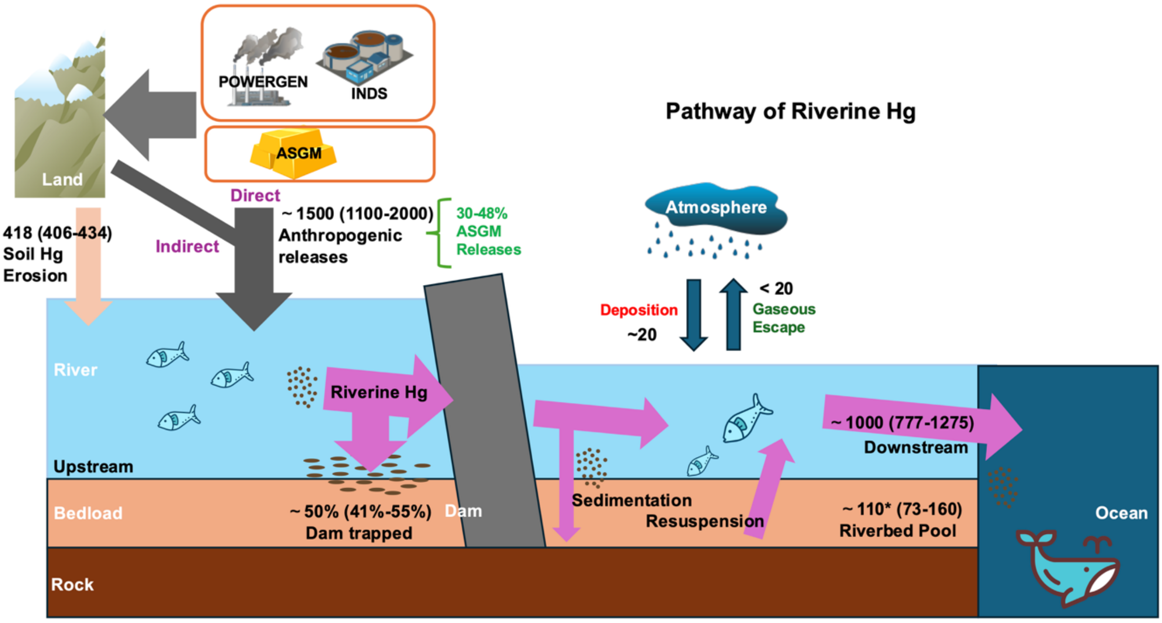

Fig. 1 Pathways and fluxes of Hg in global rivers in 2010 under different release scenarios (unit: Mg/yr). Values in parentheses indicate the range around the mean. An asterisk (*) denotes riverbed Hg pools at the end of the 10-year simulation (excluding reservoirs), expressed in Mg. Anthropogenic Hg release categories include industrial activities (INDS), energy production (POWERGEN), and artisanal and small-scale gold mining (ASGM).

Our modeling effort provides a global pattern of riverine Hg, including its sources, transport, and fate under different release scenarios (Fig. 1). Previous estimations by Streets, et al. [15], indicated that global anthropogenic Hg releases to land and water are in total at ~ 7,300 Mg/yr (mean) in 2010. In this study, our results of baseline simulation suggested that about 20% of this amount enters river systems, amounting to roughly 1,500 Mg/yr (mean, different release scenarios ranging from 1,100 to 2,000 Mg/yr) (Table 3). This magnitude may be reflected in recent isotope-based source-tracking studies [48]. Of these human-induced Hg releases to rivers, 30%-48% originate from ASGM under different release scenarios. The gross Hg inputs to rivers under the Baseline scenario, consists of erosional and human-induced Hg releases, total approximately 1,900 Mg/yr, with around 30% of this contributed by erosional soil Hg fluxes (~420 Mg/yr). Long-term legacy Hg sources from floodplains are accounted for through either erosion or river sediment resuspension processes, depending on whether the floodplains are submerged. Hg contamination from releases to land, such as historical Hg inputs to soils, are represented by present-day soil Hg concentration datasets [36, 37]. We also tested the effect of dynamic soil Hg concentrations driven by Hg deposition (+) and soil erosion (–) (refer to *Deposition Experiment*, Table 1). The results show that incorporating short-term Hg deposition produces riverine Hg budgets to the ocean is similar to those obtained under the assumption of constant soil Hg concentrations (differences <5%, Fig. S5). However, using the assumption of constant soil Hg concentration significantly reduces computational resources when running high-resolution simulations with CESM2, hence we use a constant soil Hg assumption in the major simulations.

Atmospheric Hg deposition has limited short-term impacts on erosional Hg fluxes through changes in soil Hg concentration in the watershed, indirectly increasing erosional Hg align with the increasing soil Hg over time (refer to Uncertainty analysis, *Deposition Experiment*). The long-term impacts of atmospheric Hg deposition on the watershed are accounted for in this simulation through the incorporation of soil Hg concentration changes from pre-industrial to the present-day by using a dataset of the present-day soil Hg concentration. Due to the barrier effect of dams and reservoirs, 41-55% of riverine Hg settles with sediments in these reservoirs (Table 3). Riverine Hg originating from ASGM sources has a higher likelihood of reaching the oceans, as reservoirs and dams are more strongly associated with industrial activity (e.g., regions with greater hydropower development and industrial infrastructure). As a result, the trapping efficiency is lower for ASGM-derived Hg, with a ~7% reduction in trapping rate under the High ASGM Release scenario compared to the *High Industrial Release* scenario (Table 3).

In our simulations, contemporary atmospheric Hg deposition to the global land surface contributes an additional ~20 Mg/yr of terrestrial Hg inputs to rivers, as represented in the Deposition experiments. This contribution is negligible compared to other Hg sources (anthropogenic or erosional Hg) and primarily reflects a short-term legacy effect of recent atmospheric deposition. The established literature demonstrates that the global net air-water exchange over lotic systems is directed from the atmosphere into the water [33, 49]. Constrained by this net-depositional gradient and the magnitude of the atmospheric-derived terrestrial inputs, we deduce that gross gaseous Hg evasion from the river surface is minimal, bounded at less than 20 Mg/yr across the air-water interface. In-stream Hg sedimentation is computed dynamically from sediment fluxes and particulate Hg concentrations, explicitly accounting for resuspension during high-flow events. Over the short-term 10-year simulation period, approximately 110 Mg (mean) of Hg is deposited in riverbeds.

Riverbed Hg constitutes a transient sink, easily mobilized by high-flow flood pulses. Notably, in-stream sedimentation remains substantially lower than reservoir trapping. This disparity is strictly hydrodynamic; free-flowing rivers maintain sufficient transport capacities to suspend particulate Hg, whereas reservoirs drastically reduce flow velocities, forcing highly efficient sediment and Hg settling. Ultimately, riverine Hg export to the oceans, defined as the net flux leaving each river network, reaches approximately 1,000 (mean, range from 777 to 1,275) Mg/yr.

3.2 Hg inputs to the global rivers

The input of Hg to rivers is mostly contributed by soil erosion processes and human-induced releases, with the latter acting as the predominant source during the present-day (Fig. 1, 2). Human-induced soil erosion, such as that resulting from deforestation, and long-term soil Hg accumulation, such as centuries of Hg deposition, are included in the soil Hg erosion process. In contrast, short-term contaminated soil erosion, for example Hg deposited on land and subsequently mobilized into rivers within a single year, is treated as part of the human-induced Hg releases process. We consider the *Baseline Scenario* (based on the *revised AMAP release* scenario) wherein the gross anthropogenic Hg releases to rivers is 1,500 Mg/yr, representing the present-day conditions (with ~1,000 Mg/yr, mean, global riverine Hg export fluxes from rivers to oceans by Liu, et al. [1], Table 2). We categorize anthropogenic Hg releases into two categories to align with the AMAP inventory [42, 47], including Industrial and ASGM (Fig. 2). The spatial distributions of anthropogenic Hg sources in North America are based on the Streets inventory [43], with other continents on the AMAP inventory (refer to Methods). Hence, the higher industrial Hg releases are mostly located in East Asia, South Asia, North America, West Europe, and part of South Africa, which are aligned with atmospheric Hg emissions (Fig. 2a). The ASGM Hg releases are mostly located in South and Central America, Southeast Asia, and South-Central Africa (Fig. 2b).

The contribution of soil Hg erosion to riverine Hg is relatively small (Fig. 2c) and influenced by factors such as precipitation, vegetation, soil characteristics, slope, and runoff [2, 25, 50]. In general, erosional Hg contributes 418 (406–434) Mg/yr to global rivers across the different release scenarios. This flux is independent of anthropogenic Hg releases and dam trapping processes, as erosion is parameterized as a separate natural pathway. Its spatial distribution and amounts are consistent with that simulated in our previous study for the pre-industrial period while with ~400 Mg/yr (mean) [25]. Comparing pre-industrial and present-day simulations, we align land use, land cover, soil Hg, and land surface datasets with their respective periods to ensure consistent representation of erosional Hg fluxes across different time slices. The resulting difference in erosional Hg between the two periods is small (~20 Mg/yr, mean), indicating limited sensitivity to elevated soil Hg stocks and climatic variations at the global scale. Regions adjacent to plateaus have higher erosional Hg fluxes, such as those near the Tibetan Plateau in East Asia, and South Asia, as well as areas near mountains, such as those on the west coast of South America near the Andes Mountains. The model also simulates higher Hg erosion flux in the Amazon watershed during the present-day (39.2 Mg/yr, mean) rather than at the pre-industrial era (26.2 Mg/yr, mean) due to deforestation in the region [25]. The change in erosional Hg flux from the pre-industrial era to the present day is approximately 33% (mean) relative to present-day levels. This magnitude is consistent with the business-as-usual projection in Amazon by 2050 reported by Feinberg et al. [51], which also shows an increase of about 33% compared to present-day conditions. The simulated erosional Hg flux to rivers in Europe (including the UK) is approximately 1.3 Mg/yr (mean), which is lower than the previous estimate of 5.9 Mg/yr (mean) reported by Panagos, et al. [52]. This discrepancy may stem from the coarse resolution of our simulation and the inclusion of mixed anthropogenic Hg contributions (such as agriculture) from earlier estimation [52].

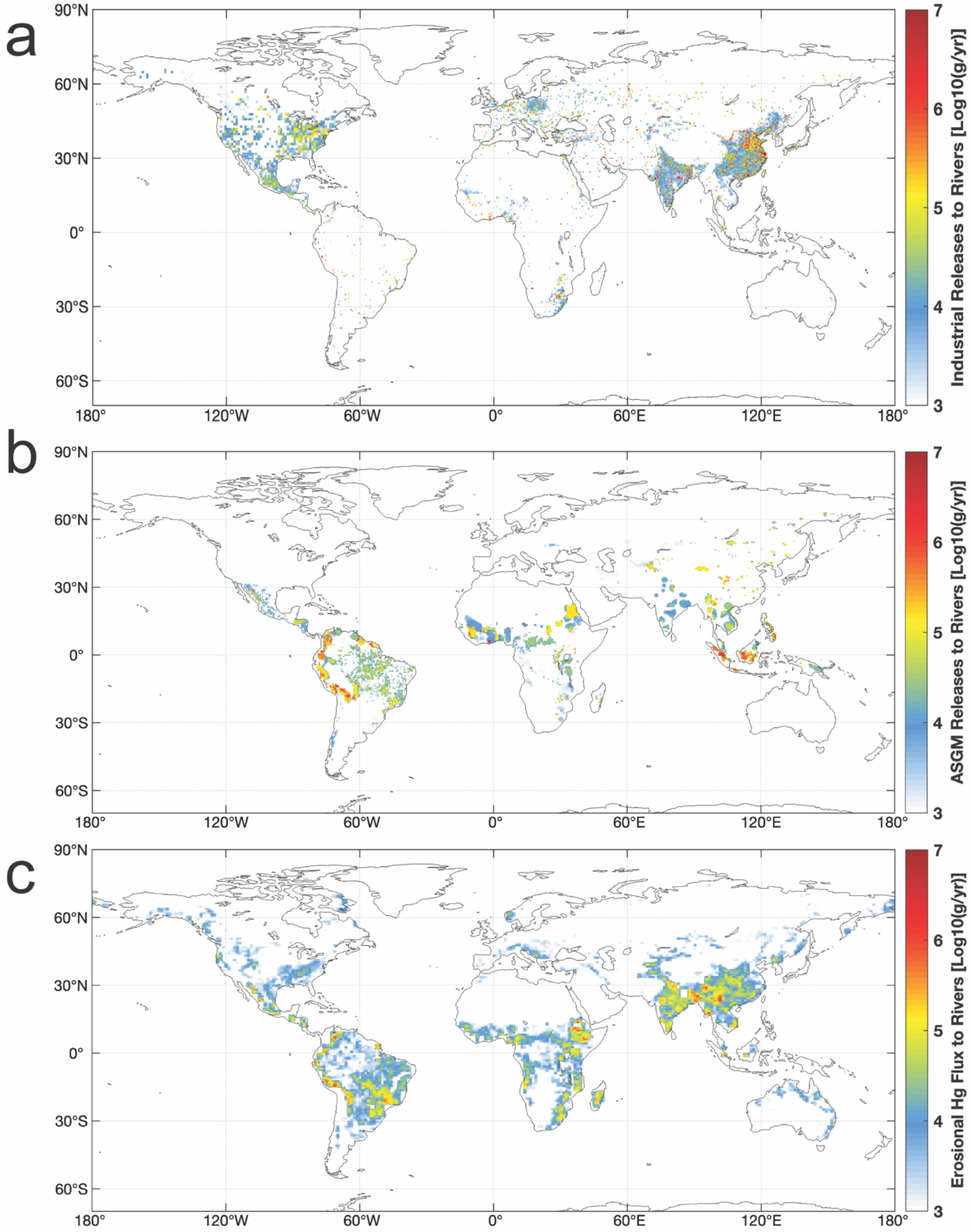

Fig. 2 Input of Hg to global rivers. a) Industrial releases to rivers, b) artisanal and small-scale gold mining (ASGM) releases to rivers, c) Erosional Hg flux to rivers. Each data point represents a 0.5° × 0.5° latitude-longitude grid cell; therefore, Hg releases below 10^3 g/yr may be reported as zero.

3.3 Impacts from reservoirs/dams to riverine Hg

Our findings suggest that reservoirs/dams can largely influence the global gross riverine Hg budget by reducing transport flux by 40-50% (Fig. 1, 3). These Hg trapping rates are consistent with previous estimates of global sediment retention (~50%, mean) [53, 54]. This agreement supports the robustness of the modeled Hg trapping estimates, given the similar transport behavior of Hg and sediments, particularly the dominance of particulate-bound Hg in rivers. The Hg form may change after settling into the bed of reservoirs, because of methylation and/or change to the dissolved phase, but in this study, we assume the Hg fluxes are only impacted by resuspension at this stage due to the relatively smaller fluxes related to the biological and other activities [55]. Reservoirs and dams play roles in reducing riverine Hg transport fluxes and SPM in the downstream portions of rivers [53, 54]. These are important components of spatial variabilities for riverine Hg transport fluxes along channels. The increasing trend of Hg flux from upstream to downstream can be interrupted by reservoirs and dams, which trap Hg from upstream input and sharply decrease the flux. The Hg flux increases from the decreased levels downstream of a dam to higher levels before reaching the next dam.

In the presence of reservoirs, total riverine Hg export fluxes to the oceans decrease by 41% (mean) under scenarios without anthropogenic Hg releases, declining from 417 Mg/yr (*NHHR wt R*) to 248 Mg/yr (*NHHR w R*). If we consider both the erosional Hg inputs and anthropogenic Hg releases, reservoirs/dams reduce Hg fluxes to oceans by 50% from 2,021 Mg/yr (*BHHR wt R*) to 1,014 Mg/yr (*BHHR w R*). The difference between the two pairs of runs reflects the large regional variabilities associated with the impact of reservoirs (Fig. 3bd). When examining specific case studies of anthropogenic Hg releases (*BHHR w/wt R*), the riverine Hg exports of Yangtze, Yellow, Parana, and Niger River have been reduced by 77%, 75%, 63% and 61%, respectively. This variability in Hg reduction at the local level is a reflection of the number of reservoirs or/and the portion of mega reservoirs such as the Three Gorges Dam, and Aswan High Dam. Indeed, some rivers show limited impacts from water management if there are fewer reservoirs and/or fewer mega reservoirs along the river. For example, the Congo River, Amazon River, and Ganges-Brahmaputra Delta have experienced reductions in riverine Hg export fluxes of <1%, 1%, and 17%, respectively. As for the no human-induced Hg release scenarios, the pattern is similar to the above regions (Fig. 3bd).

Reservoirs regulate river flooding and consequently the seasonal fluctuations of Hg fluxes, even though we assume the human-induced Hg releases to rivers are constant during the various seasons in the simulations. For example, flood pulses driven by increased runoff and larger soil erosional fluxes during the wet season contrast with reduced fluxes during the dry season, thereby altering soil Hg erosion fluxes. The differences between monthly global Hg exports have been reduced from 22.0-52.5 Mg/month (minimum to maximum, *NHHR wt R*) to 12.5-29.3 Mg/month (*NHHR w R*) with the amplitude reduced by 45% from 30.6 to 16.8 Mg/month. The monthly Hg export also decreased from 150.3-196.6 to 74.6-94.3 Mg/month under the *BHHR w/wt R* with amplitude reduced by 58% from 46.3 to 19.7 Mg/month. The trapping effects of dams are more pronounced in the Northern Hemisphere (Fig. 3ef), attributed to the larger landmass, and numbers of rivers and reservoirs as compared to the Southern Hemisphere [35, 56]. Furthermore, this effect is amplified by the larger anthropogenic Hg releases, leading to obvious differences in riverine Hg export fluxes during summer in the Northern Hemisphere (Fig. 3e). In conclusion, the reservoirs/dams reduce the effects of the seasonal change of riverine Hg.

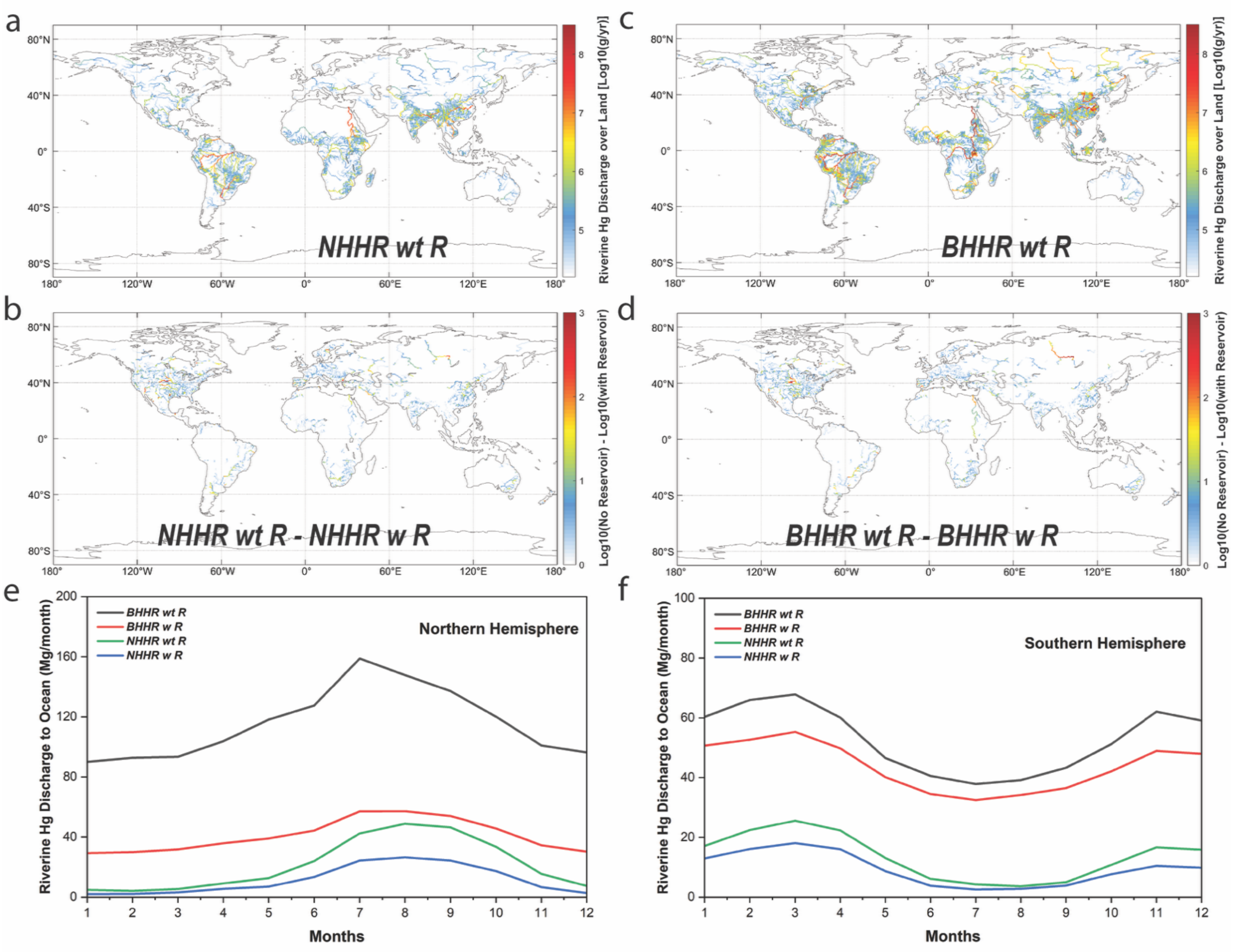

Fig. 3 Impact of reservoir and dams on riverine Hg transport. a) Riverine Hg transport fluxes in global rivers under *No Human-induced Hg Release without Reservoir scenario (NHHR wt R)*, b) Differences of riverine Hg transport fluxes between *No Human-induced Hg Release with/without Reservoir (NHHR w/wt R)*, c) Riverine Hg transport fluxes in global rivers under *Baseline Human-induced Hg Releases without Reservoir scenario (BHHR wt R)*, d) Differences of riverine Hg transport fluxes between *Baseline Human-induced Hg Releases with/without Reservoir (BHHR w/wt R)*, e) Monthly riverine Hg export fluxes to oceans in Northern Hemisphere, f) Monthly riverine Hg export fluxes to oceans in Southern Hemisphere. Each data point represents a 0.5° × 0.5° latitude-longitude grid cell.

3.4 River Hg transport fluxes and export fluxes

The modeled global riverine Hg export fluxes to oceans/lakes is ~1,000 Mg/yr (mean) in the *Baseline scenario (also the BHHR w R)* (Fig. 1, 2). This export demonstrates pronounced spatial variability, with significantly higher fluxes discharged along the coasts of Asia and South America compared to other global regions. The top ten largest riverine Hg exporters contribute 51% (506 Mg/yr, mean) of the global discharge, with the highest rivers including the Amazon (202 Mg/yr, mean), followed by the Congo (87 Mg/yr, mean), Yangtze (52 Mg/yr, mean), and Ganges-Brahmaputra Delta (51 Mg/yr, mean) (Fig. 4). These large rivers dwarf the export fluxes from smaller rivers in these regions (less than 30 Mg/yr), especially along the north coast of South America, the Indian Peninsula, eastern China, and Southeast Asia. The denser river networks in East Asia, South America, and Central Africa could result in higher export Hg fluxes to oceans due to the joining of the rivers within the large watershed. For example, the Ganges River and the Brahmaputra River share the same estuary.

The modeled riverine Hg transport fluxes exhibit large spatial variations and seasonal variabilities (Fig. 4 and S1). Generally, Hg transport flux in many watersheds increases downstream along the main channel as tributaries merge, reaching their maximum at the river mouths, if there are no major dams. This pattern reflects the continuous input of Hg from wastewater and soil erosion in their watersheds and the high transport efficiency of SPM by rivers [25]. For example, riverine transport Hg fluxes increase in the upstream stretches of Three Gorges Dam (0-24 Mg/yr), and this trend resumes downstream of the Three Gorges Dam in the channels of Yangtze River (4-52 Mg/yr) (Fig. 4). The Panama and Mekong Rivers also have increased riverine transport Hg fluxes along the channels and reach a maximum flux at the river mouth, but this trend is less influenced by dams.

Rivers with higher anthropogenic releases and/or erosion in their watersheds can easily maintain higher Hg transport fluxes in their channels, such as the Amazon, Congo, Yangtze Rivers, and Ganges-Brahmaputra Delta (Fig. 2 and 4). For example, the highest riverine transport Hg flux in the Amazon River (Mean = 201.7 Mg/yr near its mouth) is caused by the effect of ASGM releases and erosional Hg flux to the watershed (152.5 and 32.2 Mg/yr, mean, respectively). However, industrial Hg releases in the Amazon watershed are below 10 Mg/yr. As a result, the total Hg inputs to the Amazon watershed (152.5 + 32.2 + 10 = 194.7 Mg/yr, and nearly 50% trapping by reservoirs) are lower than the simulated riverine Hg export to the ocean (201.7 Mg/yr, mean). This imbalance suggests additional contributions from internal remobilization (e.g., resuspension of riverbed sediments) and/or external Hg inputs from upstream or adjacent regions that are not fully accounted for within the watershed budget. Similarly, ASGM Hg releases contribute substantially to both riverine transport and export fluxes in the Congo River. In contrast, higher riverine export Hg fluxes of the Yangtze River (52 Mg/yr at the mouth, mean) and Ganges-Brahmaputra Delta (51.2 Mg/yr at the mouth, mean) are caused by the higher industrial releases (100.7 and 37.8 Mg/yr, mean, respectively) and erosional Hg flux (from Himalayas to the ocean; 23.6 and 49.6 Mg/yr, mean, respectively) in these regions. Indeed, the watershed of the Yangtze River includes the most industrialized regions of eastern China (Fig. 2a). Interestingly, some smaller rivers with relatively limited watershed areas, such as the Kapuas River (14.6 Mg/yr at the mouth, mean), exhibit comparatively high riverine Hg export fluxes due to intense ASGM activity (Figs. 2b, 4), consistent with findings from local studies [57].

Riverine export Hg fluxes estimated by the model agree well with the observation of riverine Hg export fluxes in river mouths (Fig. 4b). The observational dataset includes 44 rivers from various continents spanning five orders of magnitudes with a mean flux of $1\times10^{3.99\pm3.9}$ kg/yr. The model (mean flux is $1\times10^{3.90\pm3.7}$ kg/yr) represents the observations with a high coefficient of determination ($R^2 = 0.97$, $p<0.01$, Fig. 4b). The model results of riverine Hg export fluxes agree well with observation records for many major rivers, such as the Yangtze (model vs. observation: 52 vs. 48 Mg/yr, mean), Ob' (3.2 vs. 2.4 Mg/yr, mean). Although the model has performed well in simulating erosion of the small rivers [30], because of coarse anthropogenic releases, the model has a higher bias for smaller rivers, such as the Kolyma (model vs. observation: 4.7 vs. 1.1 Mg/yr, mean), Mackenzie (2.6 vs. 0.6 Mg/yr, mean) and Yukon Rivers (3.8 vs. 0.9 Mg/yr, mean). These rivers exhibit relatively lower riverine export Hg fluxes compared to larger rivers but are more sensitive to anthropogenic Hg releases within their watersheds. Even small increases in anthropogenic Hg input can substantially elevate the Hg concentrations and fluxes of smaller rivers. For instance, discrepancies in releases in large watersheds may be mitigated by the average effect among grids (and/or tributaries) with the same watershed, but such an effect is less likely to occur in smaller watersheds. Furthermore, the model agrees with observed riverine Hg transport fluxes along river channels, although such observations are available for only a limited number of major rivers. For example, the model (24 Mg/yr, mean) closely resembles the observation (26 Mg/yr, mean) from the upstream portions of the Three Gorges Dam, as well as reaches immediately downstream (4.7 and 4.4 Mg/yr, mean) [20].

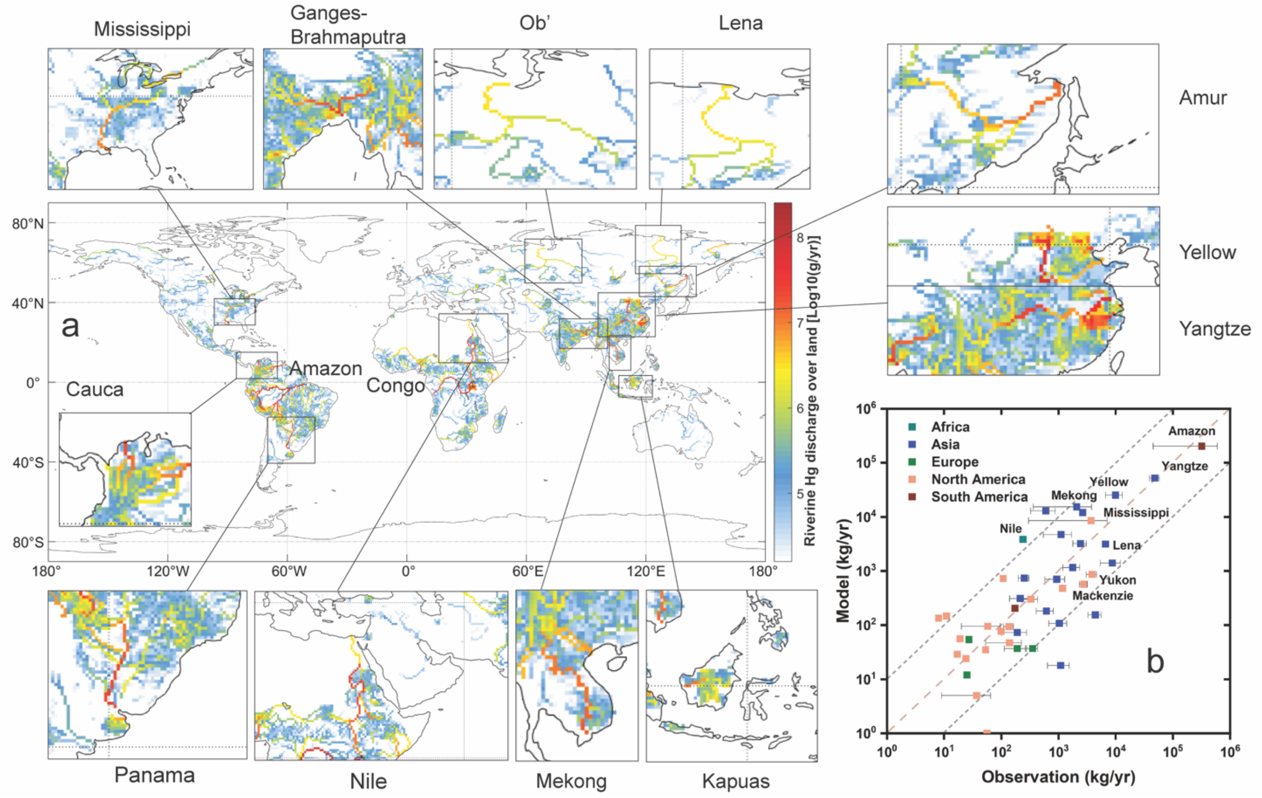

Fig. 4 Riverine transport and export Hg fluxes in global rivers. a) Spatial patterns of riverine Hg transport fluxes with zoomed regions of major rivers; b) Model results of riverine Hg export fluxes versus observation records in continents. Each data point represents a 0.5° × 0.5° latitude-longitude grid cell.

3.5 Impacts of Human-induced Hg Releases

By comparing riverine Hg input and export fluxes across different release scenarios, we assess how rivers respond to variations in both the magnitude and sectoral composition of anthropogenic Hg releases. The results show that higher anthropogenic Hg releases lead to increased riverine Hg transport and export to the oceans (Fig. 5e-g). Higher anthropogenic Hg releases increase Hg inputs to rivers, whereas the contribution from soil erosion remains stable across scenarios because initial soil Hg conditions and climatic forcing are identical during the simulations. Note that the release scenarios isolate only annual anthropogenic Hg inputs to rivers; their long-term effects on soil pools and broader Earth system components are not represented in the short-term simulations conducted in this study. The fate of Hg released from anthropogenic sectors, including riverine inputs and export to the oceans, varies across scenarios. For instance, despite comparable levels of total releases between *High Industrial Release* and *High ASGM Release scenarios*, the former exhibits a lower export fraction (Fig. 5f). With the *Moderate Release scenario* as a reference, only

28% of the increased industrial releases are ultimately transported to oceans for the *High Industrial Release* scenario (Table 3), but 54% exported for the *High ASGM Release scenario*.

Higher industrial releases contribute to higher riverine Hg export fluxes in the rivers of East Asia and Southeast Asia, while increased ASGM releases contribute to the higher riverine Hg export fluxes in the Amazon River Watershed, Central Africa, and Southeast Asia (Fig. 5). These differences in the riverine Hg transport and export fluxes are attributed to the differing water management strategies in various regions. For instance, the Amazon River has relatively more active ASGM activities and fewer reservoirs/dams and/or fewer mega reservoirs/dams in its watershed, causing higher export fractions [58]. In contrast, the Yangtze River has higher industrial releases in its watershed and impacts from reservoirs and dams (Fig. 3b). Indeed, regions with many industries often implement more extensive water management practices to provide water and hydroelectricity for reservoirs [59]. This shift in water management could result in lower riverine Hg export fractions of industrial releases in those regions (Fig. 5g).

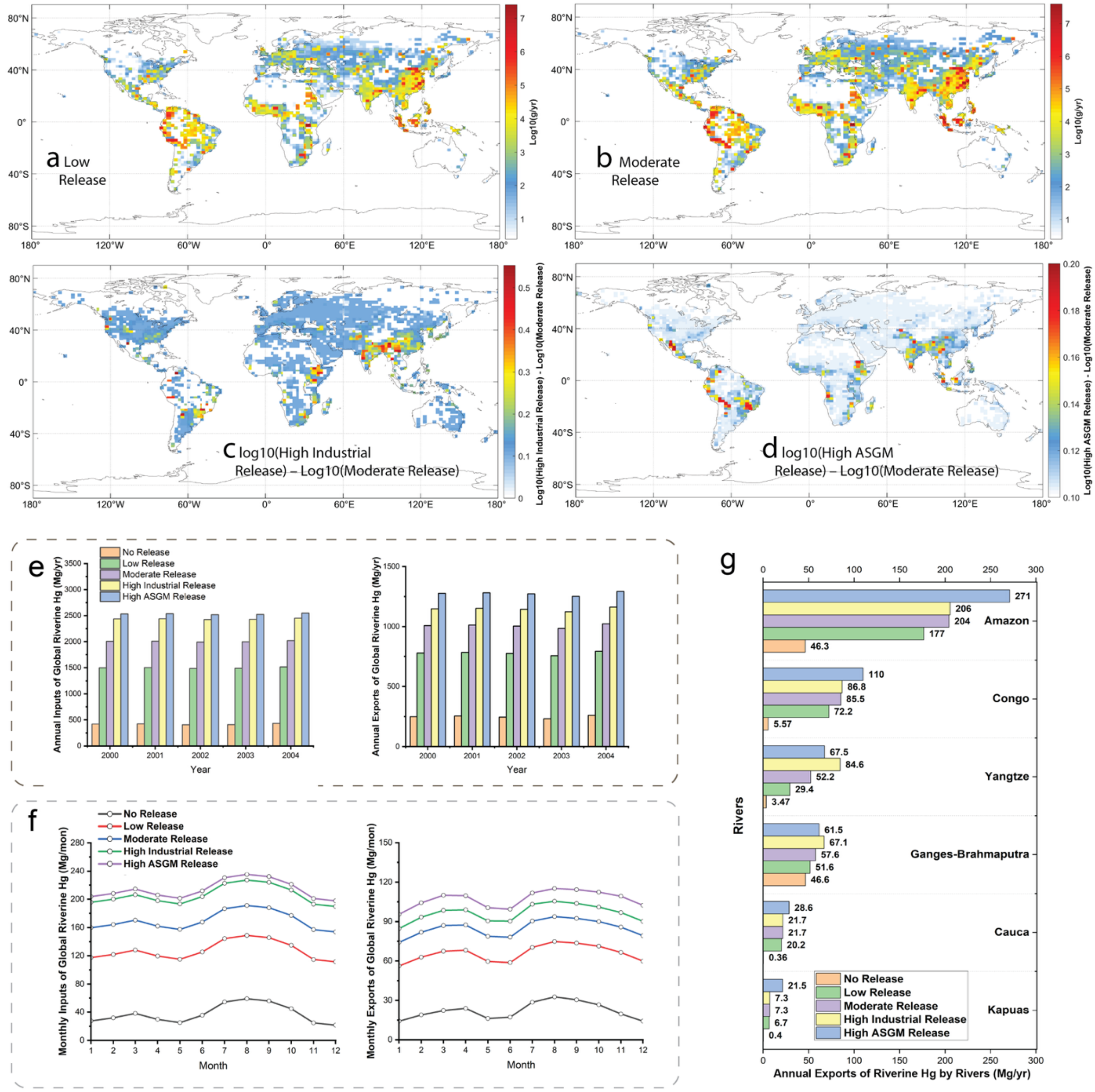

Fig. 5 Impacts of anthropogenic Hg releases on riverine Hg fluxes under different release scenarios. a) Anthropogenic Hg releases under the Low Release scenario; b) anthropogenic Hg releases under the Moderate Release scenario; c) differences in anthropogenic Hg releases between the High Industrial Release and Moderate Release scenarios (log10 scale); d) differences in anthropogenic Hg releases between the High artisanal and small-scale gold mining (ASGM) Release and Moderate Release scenarios (log10 scale); e) annual Hg inputs and outputs in global rivers; f) monthly Hg inputs and outputs in global rivers; and g) annual exports of riverine Hg to the oceans for selected rivers.

3.6 Sink of Hg in Reservoirs/Dams

Increased Hg releases from human activities lead to higher Hg accumulation rates in reservoirs, which is the major sink for riverine Hg (Fig. 1, 6). Globally, Hg accumulation rates in reservoirs rise approximately 6-fold from 14 Mg/month (mean) in the *No Release scenario* (representing pre-industrial era) to 84 Mg/month (mean) in the *Baseline Release scenario* (representing present-day). The contribution of different sectors (e.g., industrial vs. ASGM sources) to Hg releases has a smaller effect on accumulation rates than riverine Hg transport and export fluxes, as shown by similar rates in the *High Industrial Release* (106 Mg/month, mean) and *High ASGM Release* (104 Mg/month, mean) scenarios. Because human-induced Hg releases are assumed to remain constant throughout the year and dominate over natural sources, the overall increase in Hg accumulation exhibits limited seasonal variation (Fig. 5f). Differences among release scenarios on seasonal timescales are instead controlled mainly by variability in erosional Hg fluxes. As a result, anthropogenic inputs generate relatively stable monthly fluxes (Fig. 6a). Reservoir storage capacities are designed for water and/or sediments during construction; therefore, Hg storage capacity is not explicitly defined and remains uncertain. The storage estimates shown in Fig. 6 are thus based on an idealized representation of reservoir behavior while numbers of reservoirs assumed to be constant during simulations.

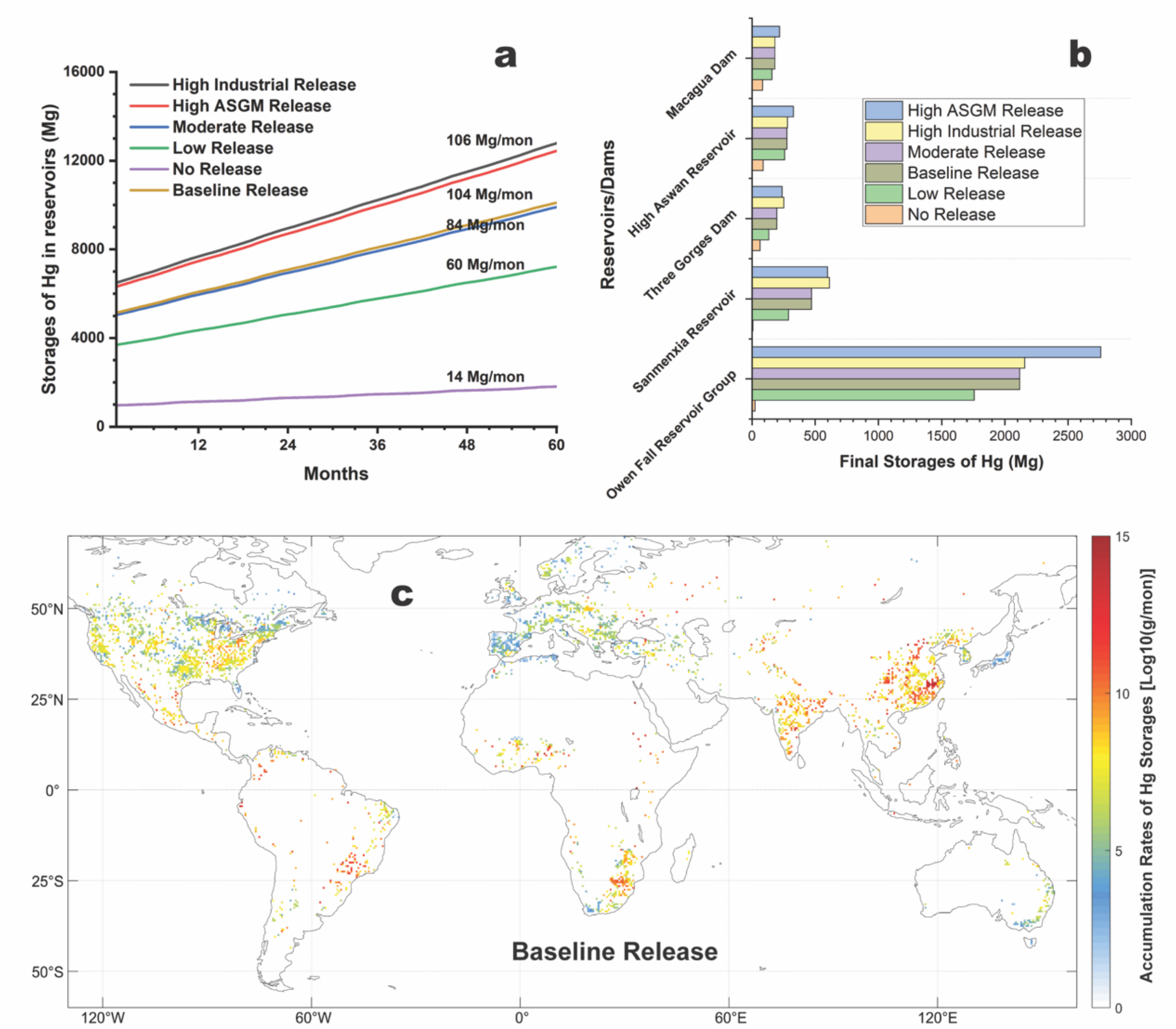

Fig. 6 Reservoir storage of riverine Hg. a) Monthly accumulation of Hg in global reservoirs; the starting point is defined by a five-year reservoir spin-up period, with reservoir Hg storage initialized to zero at the beginning of the simulation. b) Final Hg storage in large reservoirs and dams over the 10-year simulation period. c) Accumulation rates of Hg storage in global reservoirs and dams under the *Baseline Release scenario*. Note that the final Hg storage shown in panel (b) represents reservoir Hg storage at the end of the simulation period only. ASGM=Artisanal small-scale gold mining.

Reservoirs exhibit obvious regional variability in the rates of Hg accumulation, influenced by reservoir density and watershed Hg releases (Fig. 6c). In East and South Asia, higher reservoir densities combined with substantial industrial Hg releases (Fig. 2a), result in elevated Hg accumulation rates. In contrast, the United States, despite its high reservoir density, has relatively lower Hg releases (Fig. 2a, b), leading to low to moderate accumulation rates. Reservoirs in parts of Southern Africa and South America exhibit high accumulation rates, consistent with elevated Hg releases from ASGM activities (Fig. 2b, 6c). Meanwhile, Southern Europe, with a high density of reservoirs but lower regional Hg releases, shows relatively lower Hg accumulation rates.

Several specific reservoirs illustrate the dominance of human-induced Hg releases on accumulation patterns. For example, the Owen Falls Reservoir Group (upstream of the Nile), the High Aswan Dam (Nile), the Sanmenxia Reservoir (Yellow River), the Three Gorges Dam (Yangtze River), and the Macagua Dam (Caroní River) show substantial increases in Hg accumulation between *No Release* to *Low Release* scenarios, with even larger increases from *Low* to *Moderate* or *High Release* levels (Fig. 6b). Note that reservoir Hg storage is initialized to zero at the start of the 10-year simulations, and the reported values represent the accumulated storage at the end of the simulation period for each release scenario. Sectoral contributions also play a critical role: while reservoirs like the Sanmenxia and the Three Gorges experience greater accumulation under the *High Industrial Release* scenario, those such as the Owen Falls Reservoir Group see much higher accumulation rates under *High ASGM Release* scenario than the *High Industrial Release* one.

The global scarcity of continuous in-channel observations and explicit reservoir Hg flux monitoring severely limits direct large-scale model validation. For instance, while recent studies have successfully identified reservoir trapping effects by comparing Hg fluxes across different time periods [60], the absence of concurrent in-channel data prevents the precise quantification of reservoir trapping ratios. Furthermore, although detailed long-term monitoring has accurately constrained Hg pools in specific reservoirs [61], these localized systems are often too small in volume and catchment area to serve as viable comparison points for a global Earth System Model operating at ~ 1° spatial resolution.

Given these empirical limitations and the extreme rarity of comprehensive mass-balance datasets, the trapping efficiency of the few extensively monitored mega-reservoirs serves as our most viable validation proxy. For example, our simulation shows that activating the dam module reduces riverine Hg transport in the upper Yangtze River by 71% (mean). This value is consistent with field-based mass-balance estimates for the Three Gorges Dam, which indicate a persistently high trapping efficiency of around 70% (mean) across multiple monitoring years (e.g., 2016, 2018, and 2021) [2, 20]. These years are not selected to highlight a specific peak condition; rather, they are representative observations spanning different hydrological conditions, all of which consistently show similarly high retention in Yangtze watershed. The scale gap between localized biogeochemical processes and global modeling can be bridged with a concerted effort. For example, expanded global observational networks in river systems, with a critical emphasis on continuous in-channel monitoring, can help to better constrain future macro-scale assessments.

4 UNCERTAINTY ANALYSIS

The MOSART-Hg-WM model has uncertainties comparable to those in previous studies using the MOSART-Hg model [25]. We adopt the same model resolution as our previous study, which focuses on the pre-industrial era [25]. We find that the model with a higher resolution (0.5°×0.5°) performs better in simulating erosion flux in single topography units than a coarser resolution (1°×1°); however, the difference can be largely mitigated by using specific scaling factors. To balance computational cost and simulation accuracy, we use a resolution of 0.9° × 1.25°. In general, the accuracy of the erosion processes and riverine sediment/Hg delivery processes are validated against observations in previous studies [28, 29]. For instance, the model has better performance in simulating global sediment yield compared to alternative models such as the RUSLE model, with a 59% (mean) lower discrepancy relative to observations [29]. Additionally, sediment fluxes in the MOSART-Hg demonstrate similar performance to the BQART model [25].

The water management component (reservoirs/dams) accounts for sediment and riverine Hg trapping effects, alongside their influences on flow processes, which is supported by empirically validated relationships between reservoir properties and river parameters [22] (refer to Methods). The theoretical basin trapping by this method agrees well with the observed values, such as the Nile (observed 100% vs. theoretical 99%, mean), Kizil Irmak (observed 98% vs. theoretical 95%, mean) and Krishna River (observed 75% vs. theoretical 70%, mean) [22]. The water management module has also been validated independently in previous studies [26, 28]. Sediment flux estimations in MOSART-Hg-WM exhibit high performance compared to previous estimations [54] (Fig. S2). A similar level of model accuracy is expected for the Hg-trapping effects of reservoirs and dams.

Another source of uncertainties is the spatial distribution of anthropogenic Hg sources to freshwater environments. We consider two different atmospheric Hg inventories, AMAP inventory [42, 47] and Streets inventory [43], as a proxy for the spatial distribution of anthropogenic releases to rivers. The riverine Hg export fluxes from both scenarios (*AMAP scenario* and *Streets scenario* hereafter) exhibit a strong correlation with observations at a global scale (Fig. S3). However, the different spatial distributions of Hg sources result in varied performances in different regions. The *Streets scenario* has a better performance in simulating riverine Hg in North America, while the *AMAP scenario* performs better in other regions, particularly due to the more detailed sector contributions for the latter.

The soil Hg concentration datasets play a crucial role in the Hg erosion processes. The diverse datasets (Wang dataset and Liu dataset, refer to Method) exert limited impacts on global-scale riverine Hg export fluxes, with the Liu dataset resulting in only a slight increase in riverine Hg export to oceans (<10%) than using the Wang dataset. Furthermore, the *Deposition Experiment* is devised to assess uncertainties arising from the change of soil Hg concentrations due to atmospheric Hg deposition and the loss of soil Hg by erosion (Table 1). In this experiment, soil Hg concentrations are dynamically adjusted based on the atmospheric deposition and erosion processes. However, the disparities between the scenarios with constant and dynamic soil Hg concentrations are minimal, with changes in riverine Hg export to oceans < 2% (Fig. S4). Similarly, given that the rates of gaseous Hg evaporating from rivers are lower than the atmospheric Hg deposition rates [33], the combined uncertainties from gaseous Hg evaporating and deposition are expected to remain within 2%.

The transformation of Hg forms in riverine processes is not explicitly accounted for in our model, and the assumption that all Hg exists in the particulate phase leads to an overestimation of both Hg trapping in reservoirs and anthropogenic Hg releases to rivers. Directly applying empirical particulate Hg fractions is unfeasible. Our macro-scale model cannot resolve dynamic local partitioning covariates like pH or DOC, and extrapolating spatially biased observations would introduce unacceptable uncertainties. To address this uncertainty, we set up two scenarios for estimates: (1) 70% Particulate Hg: Based on observations from the Yangtze River and controlled ecosystem experiments, this scenario represents a lower bound; (2) 90% Particulate Hg: Based on observations from the Yukon River and prior estimates by Amos, et al. [19], this scenario represents an upper bound.

The results show that under the 70% and 90% particulate-phase scenarios, anthropogenic Hg releases are approximately 1,236 Mg/yr (mean) and 1,405 Mg/yr (mean), respectively, assuming a riverine Hg export of ~1,000 Mg/yr (mean) to oceans. Our estimated range of anthropogenic Hg releases (1,100–2,000 Mg/yr) effectively captures these uncertainties. The corresponding trapped Hg pools in reservoirs and dams are ~552 Mg/yr (mean) and ~792 Mg/yr (mean), respectively, which are lower than the ~900 Mg/yr (mean) estimated under the 100% particulate-phase assumption. Additionally, if anthropogenic Hg releases are held constant at ~1,500 Mg/yr, the riverine Hg export fluxes to oceans under the 70% and 90% particulate-phase scenarios are ~1,160 Mg/yr (mean) and ~1,052 Mg/yr (mean), respectively. Overall, the uncertainties arising from changes in Hg forms in our simulations have a limited impact on the global riverine Hg transport and export flux. Furthermore, the proportion of particulate-phase Hg in global rivers varies and is influenced by factors such as organic carbon content and pH [62]. Thus, incorporating biogeochemical cycling within an Earth system model can help improve riverine Hg estimates, however, which is currently absent in our approach. Details of these calculations are provided in Text S1.

5 ENVIRONMENTAL IMPLICATIONS

Anthropogenic Hg releases dominate riverine Hg delivery from upstream to downstream and export into inland lakes and/or oceans [11, 63]. However, measuring riverine Hg fluxes is challenging due to rapid changes in runoff parameters and considerable variability in Hg concentrations worldwide. The lack of historical data also hinders the proper evaluation of the trends of riverine Hg export and the contribution of anthropogenic Hg releases, posing management challenges, particularly for international rivers such as the Mekong, Jordan, Indus, Niger, and Nile Rivers [64, 65]. Our estimation provides insights into understanding regional contributions of anthropogenic Hg releases to downstream rivers and oceans. The Hg concentrations in the rivers have a strong connection to the levels of fish Hg [66, 67], hence our simulations could help to understand the Hg pollution status in the rivers and coastal environment, which is vital for fishing and aquaculture. Due to the unique environment of estuaries, where freshwater mixes with saltwater, most particulate-phase Hg settles in this region before transport along the coastline under the influence of physical forces, including the Coriolis effect [68]. Previous studies estimate Hg burial in global continental shelf regions at ~1,290 Mg/yr (mean) [69], with riverine inputs representing a major contributing source to coastal Hg sedimentation [1]. Higher riverine Hg fluxes under High anthropogenic Hg release scenarios would enhance Hg burial in coastal systems, potentially creating additional hotspots for Hg methylation and accumulation within coastal food webs.

Our assessments emphasize the role of dams/reservoirs as the sink in global Hg biogeochemistry. The accumulation of Hg in global reservoirs adds complexity to environmental governance efforts. In the short term, Hg pools increase through particulate sedimentation, while transformations such as changes in Hg speciation and bioavailability can reduce the mobile fraction. Despite high Hg levels, reservoir trapping efficiency remains largely unaffected, as it is driven primarily by sediment accumulation rather than Hg content. Over the long term in some reservoirs, Hg buried in deeper sediment layers, with limited exchange with bottom waters and have no possibility to be resuspended, can be considered effectively sequestered, particularly in deeper or smaller reservoirs, provided dredging does not occur. Management actions such as dredging can help remove sediment-bound Hg from the riverbed, reducing its potential remobilization into the aquatic system. The settled Hg in reservoirs creates a suitable environment for Hg methylation [70-72], with conditions similar to those of nutrient-rich wetlands that support biological activity and methylation.

Our findings provide insights into the size and behavior of Hg pools in global reservoirs, which can be used to assess methylation risks for human health and inform future monitoring efforts. Hg pollution has long been recognized as a sustainability challenge [73, 74], particularly because riverine Hg contamination poses direct threats to multiple the United Nations Sustainable Development Goals (SDGs) (https://www.undp.org/sustainable-development-goals)—notably SDG 3 (Good Health and Well-being) and SDG 6 (Clean Water and Sanitation). While water infrastructure supports agriculture, hydropower, and flood control, Hg accumulated in reservoir sediments and riverbeds can serve as secondary sources of contamination [2, 20], posing risks to both food and water security. For example, observations from the Yangtze River suggest that Hg retained in the Three Gorges Reservoir has become a downstream source of riverine Hg due to declining upstream Hg inputs [2]. Watershed management practices, such as dam construction, hydroelectric development, and water-sediment regulation, can significantly influence Hg fluxes and deposition patterns. Hydropower reservoirs may create conditions conducive to methylation [75], leading to elevated methylmercury concentrations in rivers, estuaries, and aquatic organisms [76]; while sediment flushing operations alter the downstream transport and fate of particulate-bound Hg [77].

Our model provides a process-based, spatially explicit scientific framework for assessing and managing the risks associated with Hg pollution in river systems. It supports the development of targeted mitigation strategies to reduce human exposure and promote more sustainable water infrastructure planning. In particular, our global estimates of Hg accumulation in reservoirs can inform environmental restoration efforts, enhance monitoring under international frameworks such as the Minamata Convention on Mercury, and contribute to SDG 17 (Partnerships for the Goals) (https://www.undp.org/sustainable-development-goals) by facilitating data-driven collaboration across regions. This work also offers a science-based foundation for risk assessments related to dam operation, modification, and removal, supporting integrated watershed and infrastructure management.

ACKNOWLEDGMENTS

We thank for the help from Keith Oleson, Erik Kluzek, Samuel Levis, and the DiscussCESM Forum Community. The CESM project is supported primarily by the U.S. National Science Foundation. We thank all the scientists, software engineers, and administrators who contributed to the development of CESM. Any use of trade, firm, or product names is for descriptive purposes only and does not imply endorsement by the U.S. Government.

FUNDING:

National Natural Science Foundation of China (NNSFC) grant 42177349 (ZS)

Fundamental Research Funds for the Central Universities, China grants 0207–14380188, 0207–14380168 (ZS)

“GeoX” Interdisciplinary Research Funds for Frontiers Science Center for Critical Earth Material Cycling, Nanjing University (ZS)

Collaborative Innovation Center of Climate Change, Jiangsu Province (ZS)

ZT was supported by the Earth System Model Development program areas of the US Department of Energy, Office of Science, Office of Biological and Environmental Research, as part of the multi-program, collaborative Integrated Coastal Modeling (ICoM) project (grant no. KP1703110/75415). PNNL is operated for DOE by Battelle Memorial Institute, United States, under contract DE-AC05-76RL01830.

Competing interests: All other authors declare they have no competing interests.

Data and materials availability: All data needed to evaluate the conclusions in the paper are present in the paper and/or the Supplementary Materials. All code is available at http://ebmg.online/mercury/. The datasets for model running of this study are available from the corresponding author upon reasonable request or download from CESM2 websites and E3SM websites. The raw data that support the findings of this study are available from the corresponding author upon reasonable request.

References

(1) Liu, M.; Zhang, Q.; Maavara, T.; Liu, S.; Wang, X.; Raymond, P. A. Rivers as the largest source of mercury to coastal oceans worldwide. *Nature Geoscience* **2021**, *14* (9), 672-677. DOI: 10.1038/s41561-021-00793-2.

(2) Peng, D.; Lyu, J.; Song, Z.; Huang, S.; Zhang, P.; Gao, J.; Zhang, Y. Mercury budgets in the suspended particulate matters of the Yangtze River. *Water Research* **2023**, *243*. DOI: 10.1016/j.watres.2023.120390.

(3) Obrist, D.; Kirk, J. L.; Zhang, L.; Sunderland, E. M.; Jiskra, M.; Selin, N. E. A review of global environmental mercury processes in response to human and natural perturbations: Changes of emissions, climate, and land use. *Ambio* **2018**, *47* (2), 116-140. DOI: 10.1007/s13280-017-1004-9.

(4) Mason, R. P.; Choi, A. L.; Fitzgerald, W. F.; Hammerschmidt, C. R.; Lamborg, C. H.; Soerensen, A. L.; Sunderland, E. M. Mercury biogeochemical cycling in the ocean and policy implications. *Environmental Research* **2012**, *119*, 101-117. DOI: 10.1016/j.envres.2012.03.013.

(5) Driscoll, C. T.; Mason, R. P.; Chan, H. M.; Jacob, D. J.; Pirrone, N. Mercury as a global pollutant: sources, pathways, and effects. *Environmental Science & Technology* **2013**, *47* (10), 4967-4983. DOI: 10.1021/es305071v.

(6) Schoch, N.; Glennon, M. J.; Evers, D. C.; Duron, M.; Jackson, A. K.; Driscoll, C. T.; Ozard, J. W.; Sauer, A. K. The impact of mercury exposure on the common loon (Gavia immer) population in the Adirondack Park, New York, USA. *Waterbirds* **2014**, *37*, 133-146. DOI: 10.1675/063.037.sp116.

(7) Eagles-Smith, C. A.; Ackerman, J. T.; De La Cruz, S. E.; Takekawa, J. Y. Mercury bioaccumulation and risk to three waterbird foraging guilds is influenced by foraging ecology and breeding stage. *Environ Pollut* **2009**, *157* (7), 1993-2002. DOI: 10.1016/j.envpol.2009.03.030.

(8) Zhang, Y.; Song, Z.; Huang, S.; Zhang, P.; Peng, Y.; Wu, P.; Gu, J.; Dutkiewicz, S.; Zhang, H.; Wu, S.; et al. Global health effects of future atmospheric mercury emissions. *Nature Communications* **2021**, *12* (1), Article. DOI: 10.1038/s41467-021-23391-7.

(9) Wu, Q.; Zhang, Y.; Li, P.; Fu, X.; Zhang, Q.; Wang, X.; Chen, L.; Wang, S.; Wang, F.; Feng, X. Ecosystem mercury recovery and health benefit under the Minamata Convention in a changing climate. *Reviews of Environmental Contamination and Toxicology* **2022**, *260* (1), Review. DOI: 10.1007/s44169-022-00016-8.

(10) Cain, A.; Morgan, J. T.; Brooks, N. Mercury policy in the Great Lakes states: past successes and future opportunities. *Ecotoxicology* **2011**, *20* (7), 1500-1511. DOI: 10.1007/s10646-011-0764-4.

(11) Liu, M.; Zhang, Q.; Yu, C.; Yuan, L.; He, Y.; Xiao, W.; Zhang, H.; Guo, J.; Zhang, W.; Li, Y.; et al. Observation-based mercury export from rivers to coastal oceans in East Asia. *Environmental Science & Technology* **2021**, *55* (20), 14269-14280. DOI: 10.1021/acs.est.1c03755.

(12) Schmeltz, D.; Evers, D. C.; Driscoll, C. T.; Artz, R.; Cohen, M.; Gay, D.; Haeuber, R.; Krabbenhoft, D. P.; Mason, R.; Morris, K.; et al. MercNet: a national monitoring network to assess responses to changing mercury emissions in the United States. *Ecotoxicology* **2011**, *20* (7), 1713-1725. DOI: 10.1007/s10646-011-0756-4.

(13) Streets, D. G.; Horowitz, H. M.; Lu, Z.; Levin, L.; Thackray, C. P.; Sunderland, E. M. Five hundred years of anthropogenic mercury: spatial and temporal release profiles*. *Environmental Research Letters* **2019**, *14* (8). DOI: 10.1088/1748-9326/ab281f.

(14) Kocman, D.; Wilson, S.; Amos, H.; Telmer, K.; Steenhuisen, F.; Sunderland, E.; Mason, R.; Outridge, P.; Horvat, M. Toward an assessment of the global inventory of present-day mercury releases to freshwater environments. *International Journal of Environmental Research and Public Health* **2017**, *14* (2), 138. DOI: 10.3390/ijerph14020138 (acccessed 2023/03/20/07:16:35). From 4.614.

(15) Streets, D. G.; Horowitz, H. M.; Jacob, D. J.; Lu, Z.; Levin, L.; ter Schure, A. F. H.; Sunderland, E. M. Total mercury released to the environment by human activities. *Environmental Science & Technology* **2017**, *51* (11), 5969-5977. DOI: 10.1021/acs.est.7b00451.

(16) AMAP/UNEP. Technical Background Report for the Global Mercury Assessment 2018. **2019**, *viii + 426 pp including E-Annexes*.

(17) Schuster, P. F.; Striegl, R. G.; Aiken, G. R.; Krabbenhoft, D. P.; Dewild, J. F.; Butler, K.; Kamark, B.; Dornblaser, M. Mercury export from the Yukon River Basin and potential response to a changing climate. *Environmental Science & Technology* **2011**, *45* (21), 9262-9267. DOI: 10.1021/es202068b.

(18) Emmerton, C. A.; Graydon, J. A.; Gareis, J. A. L.; St. Louis, V. L.; Lesack, L. F. W.; Banack, J. K. A.; Hicks, F.; Nafziger, J. Mercury export to the arctic ocean from the Mackenzie River, Canada. *Environmental Science & Technology* **2013**, *47* (14), 7644-7654. DOI: 10.1021/es400715r.

(19) Amos, H. M.; Jacob, D. J.; Kocman, D.; Horowitz, H. M.; Zhang, Y.; Dutkiewicz, S.; Horvat, M.; Corbitt, E. S.; Krabbenhoft, D. P.; Sunderland, E. M. Global biogeochemical implications of mercury discharges from rivers and sediment burial. *Environmental Science and Technology* **2014**, *48* (16), 9514-9522. DOI: 10.1021/es502134t.

(20) Liu, M.; He, Y.; Baumann, Z.; Zhang, Q.; Jing, X.; Mason, R. P.; Xie, H.; Shen, H.; Chen, L.; Zhang, W.; et al. The impact

of the Three Gorges Dam on the fate of metal contaminants across the river-ocean continuum. *Water Research* **2020**, *185*, 116295. DOI: 10.1016/j.watres.2020.116295.

(21) Kocman, D.; Kanduč, T.; Ogrinc, N.; Horvat, M. Distribution and partitioning of mercury in a river catchment impacted by former mercury mining activity. *Biogeochemistry* **2010**, *104* (1-3), 183-201. DOI: 10.1007/s10533-010-9495-5.

(22) Vörösmarty, C. J.; Meybeck, M.; Fekete, B.; Sharma, K.; Green, P.; Syvitski, J. P. M. Anthropogenic sediment retention: major global impact from registered river impoundments. *Global and Planetary Change* **2003**, *39* (1-2), 169-190. DOI: 10.1016/s0921-8181(03)00023-7.

(23) Sun, X.; Tian, L.; Fang, H.; Walling, D. E.; Huang, L.; Park, E.; Li, D.; Zheng, C.; Feng, L. Changes in global fluvial sediment concentrations and fluxes between 1985 and 2020. *Nature Sustainability* **2025**. DOI: 10.1038/s41893-024-01476-7.

(24) Dethier, E. N.; Renshaw, C. E.; Magilligan, F. J. Rapid changes to global river suspended sediment flux by humans. *Science* **2022**, *376* (6600), 1447-1452. DOI: 10.1126/science.abn7980.

(25) Peng, D.; Tan, Z.; Yuan, T.; Wu, P.; Song, Z.; Zhang, P.; Huang, S.; Zhang, Y.; Lei, T.; Middleton, B. A.; et al. Human perturbations to mercury in global rivers. *Sci Adv* **2025**, *11* (24), eadw0471. DOI: 10.1126/sciadv.adw0471 From NLM Medline.

(26) Zhou, T.; Leung, L. R.; Leng, G.; Voisin, N.; Li, H. Y.; Craig, A. P.; Tesfa, T.; Mao, Y. Global irrigation characteristics and effects simulated by fully coupled land surface, river, and water management models in E3SM. *J Adv Model Earth Sy* **2020**, *12* (10). DOI: 10.1029/2020ms002069.

(27) Voisin, N.; Li, H.; Ward, D.; Huang, M.; Wigmosta, M.; Leung, L. R. On an improved sub-regional water resources management representation for integration into earth system models. *Hydrology and Earth System Sciences* **2013**, *17* (9), 3605-3622. DOI: 10.5194/hess-17-3605-2013.

(28) Li, H.-Y.; Tan, Z.; Ma, H.; Zhu, Z.; Abeshu, G. W.; Zhu, S.; Cohen, S.; Zhou, T.; Xu, D.; Leung, L. R. A new large-scale suspended sediment model and its application over the United States. *Hydrology and Earth System Sciences* **2022**, *26* (3), 665-688. DOI: 10.5194/hess-26-665-2022.

(29) Tan, Z. L.; Leung, L. R.; Li, H. Y.; Tesfa, T. Modeling sediment yield in land surface and earth system models: model comparison, development, and evaluation. *J Adv Model Earth Sy* **2018**, *10* (9), 2192-2213, Article. DOI: 10.1029/2017ms001270.

(30) Tan, Z.; Leung, L. R.; Li, H. Y.; Cohen, S. Representing global soil erosion and sediment flux in earth system models. *J Adv Model Earth Sy* **2022**, *14* (1). DOI: 10.1029/2021ms002756.

(31) Sheng, M. Y.; Lei, H. M.; Jiao, Y.; Yang, D. W. Evaluation of the Runoff and River Routing Schemes in the Community Land Model of the Yellow River Basin. *J Adv Model Earth Sy* **2017**, *9* (8), 2993-3018, Article. DOI: 10.1002/2017ms001026.

(32) Li, H. Y.; Leung, L. R.; Getirana, A.; Huang, M. Y.; Wu, H.; Xu, Y. B.; Guo, J. L.; Voisin, N. Evaluating Global Streamflow Simulations by a Physically Based Routing Model Coupled with the Community Land Model. *Journal of Hydrometeorology* **2015**, *16* (2), 948-971. DOI: 10.1175/Jhm-D-14-0079.1.

(33) da Silva, G. S.; Jardim, W. F.; Fadini, P. S. Elemental gaseous mercury flux at the water/air interface over the Negro River basin, Amazon, Brazil. *Science of The Total Environment* **2006**, *368* (1), 189-198. DOI: 10.1016/j.scitotenv.2005.09.082.

(34) Mayorga, E.; Seitzinger, S. P.; Harrison, J. A.; Dumont, E.; Beusen, A. H. W.; Bouwman, A. F.; Fekete, B. M.; Kroeze, C.; Van Drecht, G. Global Nutrient Export from WaterSheds 2 (NEWS 2): model development and implementation. *Environmental Modelling & Software* **2010**, *25* (7), 837-853. DOI: 10.1016/j.envsoft.2010.01.007.

(35) Lehner, B.; Liermann, C. R.; Revenga, C.; Vörösmarty, C.; Fekete, B.; Crouzet, P.; Döll, P.; Endejan, M.; Frenken, K.; Magome, J.; et al. High‐resolution mapping of the world's reservoirs and dams for sustainable river‐flow management. *Frontiers in Ecology and the Environment* **2011**, *9* (9), 494-502. DOI: 10.1890/100125.

(36) Wang, X.; Yuan, W.; Lin, C.-J.; Zhang, L.; Zhang, H.; Feng, X. Climate and vegetation as primary drivers for global mercury storage in surface soil. *Environmental Science & Technology* **2019**, *53* (18), 10665-10675. DOI: 10.1021/acs.est.9b02386.

(37) Liu, Y.-R.; Guo, L.; Yang, Z.; Xu, Z.; Zhao, J.; Wen, S.-H.; Delgado-Baquerizo, M.; Chen, L. Multidimensional drivers of mercury distribution in global surface soils: insights from a global standardized field survey. *Environmental Science & Technology* **2023**, *57* (33), 12442-12452. DOI: 10.1021/acs.est.3c04313.

(38) Kim, H. Global Soil Wetness Project Phase 3 (GSWPv3) atmospheric boundary conditions (experiment 1). *Data Integration and Analysis System (DIAS)* **2017**. DOI: 10.20783/DIAS.501 From Data Integration and Analysis System (DIAS).

(39) Hurtt, G. C.; Chini, L.; Sahajpal, R.; Frolking, S.; Bodirsky, B. L.; Calvin, K.; Doelman, J. C.; Fisk, J.; Fujimori, S.; Klein Goldewijk, K.; et al. Harmonization of global land use change and management for the period 850–2100 (LUH2) for CMIP6. *Geoscientific Model Development* **2020**, *13* (11), 5425-5464. DOI: 10.5194/gmd-13-5425-2020.

(40) Lawrence, D. M.; Fisher, R. A.; Koven, C. D.; Oleson, K. W.; Swenson, S. C.; Bonan, G.; Collier, N.; Ghimire, B.; van Kampenhout, L.; Kennedy, D.; et al. The Community Land Model Version 5: description of new features, benchmarking, and impact of forcing uncertainty. *J Adv Model Earth Sy* **2019**, *11* (12), 4245-4287. DOI: 10.1029/2018ms001583.

(41) Horowitz, H. M.; Jacob, D. J.; Amos, H. M.; Streets, D. G.; Sunderland, E. M. Historical mercury releases from commercial products: global environmental implications. *Environmental Science & Technology* **2014**, *48* (17), 10242-10250. DOI: 10.1021/es501337j.

(42) Steenhuisen, F.; Wilson, S. J. Geospatially distributed (gridded) global mercury emissions to air from anthropogenic sources in 2015. *DataverseNL* **2022**. DOI: doi:10.34894/SZ2KOI.

(43) Streets, D. G.; Horowitz, H. M.; Lu, Z.; Levin, L.; Thackray, C. P.; Sunderland, E. M. Global and regional trends in mercury emissions and concentrations, 2010–2015. *Atmos. Environ.* **2019**, *201*, 417-427. DOI: 10.1016/j.atmosenv.2018.12.031.

(44) Wu, Q.; Tang, Y.; Wang, L.; Wang, S.; Han, D.; Ouyang, D.; Jiang, Y.; Xu, P.; Xue, Z.; Hu, J. Impact of emission reductions and meteorology changes on atmospheric mercury concentrations during the COVID-19 lockdown. *Science of The Total Environment* **2021**, *750*. DOI: 10.1016/j.scitotenv.2020.142323.

(45) Smith-Roberts, A.; Bruckner, K. D.; Bellido, V. M.; Ossandón, H. F.; Nayak, M.; Smith, N. M.; Urrego, L. J. 'All that glitters is not gold': the effects of the COVID-19 pandemic on artisanal and small-scale gold mining and supply chains in Peru. *Journal of Energy & Natural Resources Law* **2021**, *39* (4), 489-527. DOI: 10.1080/02646811.2021.1895526.

(46) Singh Malik, Y.; Ikram Ansari, M.; Gharieb, R.; Ghosh, S.; Kumar Chaudhary, R.; Gomaa Hemida, M.; Torabian, D.; Rahmani, F.; Ahmadi, H.; Hajipour, P.; et al. The Impact of COVID-19 Pandemic on Agricultural, Livestock, Poultry and Fish Sectors. *Veterinary Medicine International* **2024**, *2024* (1). DOI: 10.1155/2024/5540056.

(47) Steenhuisen, F.; Wilson, S. J. Development and application of an updated geospatial distribution model for gridding 2015 global mercury emissions. *Atmos. Environ.* **2019**, *211*, 138-150. DOI: 10.1016/j.atmosenv.2019.05.003.

(48) Tang, K.; Fu, X.; Zhang, H.; Jia, L.; Sun, G.; Sun, Y.; Zhang, H.; Feng, X. Declines in Riverine Mercury Export from China Driven by Water Pollution Controls. *Environmental Science & Technology* **2026**, *60* (9), 7123-7133. DOI: 10.1021/acs.est.5c15219.

(49) Zhang, Y.; Jacob, D. J.; Dutkiewicz, S.; Amos, H. M.; Long, M. S.; Sunderland, E. M. Biogeochemical drivers of the fate of riverine mercury discharged to the global and Arctic oceans. *Global Biogeochem Cy* **2015**, *29* (6), 854-864. DOI: 10.1002/2015gb005124.

(50) Dutta, S. Soil erosion, sediment yield and sedimentation of reservoir: a review. *Modeling Earth Systems and Environment* **2016**, *2* (3), 123. DOI: 10.1007/s40808-016-0182-y.

(51) Feinberg, A.; Jiskra, M.; Borrelli, P.; Biswakarma, J.; Selin, N. E. Deforestation as an anthropogenic driver of mercury pollution. *Environmental Science & Technology* **2024**. DOI: 10.1021/acs.est.3c07851.

(52) Panagos, P.; Jiskra, M.; Borrelli, P.; Liakos, L.; Ballabio, C. Mercury in European topsoils: Anthropogenic sources, stocks and fluxes. *Environmental Research* **2021**, *201*. DOI: 10.1016/j.envres.2021.111556.

(53) Syvitski, J. P.; Vorosmarty, C. J.; Kettner, A. J.; Green, P. Impact of humans on the flux of terrestrial sediment to the global coastal ocean. *Science* **2005**, *308* (5720), 376-380. DOI: 10.1126/science.1109454.

(54) Syvitski, J.; Ángel, J. R.; Saito, Y.; Overeem, I.; Vörösmarty, C. J.; Wang, H.; Olago, D. Earth’s sediment cycle during the Anthropocene. *Nature Reviews Earth & Environment* **2022**, *3* (3), 179-196. DOI: 10.1038/s43017-021-00253-w.

(55) Liu, M.; Xie, H.; He, Y.; Zhang, Q.; Sun, X.; Yu, C.; Chen, L.; Zhang, W.; Zhang, Q.; Wang, X. Sources and transport of methylmercury in the Yangtze River and the impact of the Three Gorges Dam. *Water Research* **2019**, *166*, 115042. DOI: 10.1016/j.watres.2019.115042.

(56) Mulligan, M.; van Soesbergen, A.; Sáenz, L. GOODD, a global dataset of more than 38,000 georeferenced dams. *Scientific Data* **2020**, *7* (1). DOI: 10.1038/s41597-020-0362-5.

(57) Baiq, D. K. ASGM status in West Nusa Tenggara Province, Indonesia. *Journal of Degraded and Mining Lands Management* **2018**, *5* (2), 1077.

(58) Tundisi, J. G.; Goldemberg, J.; Matsumura-Tundisi, T.; Saraiva, A. C. F. How many more dams in the Amazon? *Energy Policy* **2014**, *74*, 703-708. DOI: 10.1016/j.enpol.2014.07.013.

(59) Chen, J.; Shi, H.; Sivakumar, B.; Peart, M. R. Population, water, food, energy and dams. *Renewable and Sustainable Energy Reviews* **2016**, *56*, 18-28. DOI: 10.1016/j.rser.2015.11.043.

(60) Zolkos, S.; Zhulidov, A. V.; Gurtovaya, T. Y.; Gordeev, V. V.; Berdnikov, S.; Pavlova, N.; Kalko, E. A.; Kuklina, Y. A.; Zhulidov, D. A.; Kosmenko, L. S.; et al. Multidecadal declines in particulate mercury and sediment export from Russian rivers in the pan-Arctic basin. *Proceedings of the National Academy of Sciences* **2022**, *119* (14). DOI: 10.1073/pnas.2119857119.

(61) Morway, E. D.; Hirsch, R. M.; Paul, A. P.; Marvin-DiPasquale, M.; Thodal, C. E. Long-term mercury loading and trapping dynamics in a Western North America reservoir. *Journal of Hydrology: Regional Studies* **2023**, *50*. DOI: 10.1016/j.ejrh.2023.101566.

(62) Maia, P. D.; Maurice, L.; Tessier, E.; Amouroux, D.; Cossa, D.; Pérez, M.; Moreira-Turcq, P.; Rhéault, I. Mercury distribution and exchanges between the Amazon River and connected floodplain lakes. *Science of The Total Environment* **2009**, *407* (23), 6073-6084. DOI: 10.1016/j.scitotenv.2009.08.015.

(63) Yu, C. H.; Xu, Y. P.; Yan, Y. Y.; Xiao, W. J.; Liu, M. D.; Cheng, M. H.; He, W.; Xu, F. L.; Wang, X. J. Mercury and methylmercury in China's lake sediments and first estimation of mercury burial fluxes. *Science of the Total Environment* **2021**, *770*. DOI: 10.1016/j.scitotenv.2021.145338.

(64) Campbell, I. The challenges for Mekong River management. In *The Mekong*, 2009; pp 403-419.

(65) Campbell, I. C. Perceptions, data, and river management: Lessons from the Mekong River. *Water Resources Research* **2007**, *43* (2). DOI: 10.1029/2006wr005130.

(66) Scudder, B. C.; Chasar, L. C.; Wentz, D. A.; Bauch, N. J.; Brigham, M. E.; Moran, P. W.; Krabbenhoft, D. P. *Mercury in fish, bed sediment, and water from streams across the United States, 1998-2005*; Reston, VA, 2009. https://pubs.usgs.gov/publication/sir20095109DOI: 10.3133/sir20095109.

(67) Blanchfield, P. J.; Rudd, J. W. M.; Hrenchuk, L. E.; Amyot, M.; Babiarz, C. L.; Beaty, K. G.; Bodaly, R. A. D.; Branfireun, B. A.; Gilmour, C. C.; Graydon, J. A.; et al. Experimental evidence for recovery of mercury-contaminated fish populations. *Nature* **2021**, *601* (7891), 74-78. DOI: 10.1038/s41586-021-04222-7.

(68) Zhu, S.; Wu, P.; Zhang, S.; Jahn, O.; Li, S.; Zhang, Y. A high-resolution marine mercury model MITgcm-ECCO2-Hg with online biogeochemistry. *Geoscientific Model Development* **2023**, *16* (20), 5915-5929. DOI: 10.5194/gmd-16-5915-2023.

(69) Liu, M.; Zhou, C.; Zhang, Q.; Raymond, P. A.; Li, X.; Mason, R. P.; Maavara, T.; Wang, J.; Qin, H.; Shen, G.; et al. Fish trawling and climate perturbations threaten the largest marine mercury sink. *Nature Sustainability* **2025**, *8* (11), 1280-1293. DOI: 10.1038/s41893-025-01642-5.

(70) Hsu-Kim, H.; Eckley, C. S.; Achá, D.; Feng, X.; Gilmour, C. C.; Jonsson, S.; Mitchell, C. P. J. Challenges and opportunities for managing aquatic mercury pollution in altered landscapes. *Ambio* **2018**, *47* (2), 141-169. DOI: 10.1007/s13280-017-1006-7.

(71) Ma, H.; Chen, Q.; Liu, D.; Chen, Y.; Lin, Y.; Zhang, J.; Yan, X. Impacts of river damming on sediment methylmercury dynamics. *ACS ES&T Water* **2023**, *3* (4), 934-942. DOI: 10.1021/acsestwater.2c00397.

(72) Pestana, I. A.; Azevedo, L. S.; Bastos, W. R.; Magalhães de Souza, C. M. The impact of hydroelectric dams on mercury dynamics in South America: A review. *Chemosphere* **2019**, *219*, 546-556. DOI: 10.1016/j.chemosphere.2018.12.035.

(73) Sodeno, R. Analysis of the Minamata Convention on Mercury in the Context of Sustainable Development Goals (SDGs). *Global Environmental Research* **2020**, 065-070.

(74) Selin, H.; Selin, N. E. From Stockholm to Minamata and beyond: Governing mercury pollution for a more sustainable future. *One Earth* **2022**, *5* (10), 1109-1125. DOI: 10.1016/j.oneear.2022.09.001.

(75) Amyot, M.; Bilodeau, F.; Tremblay, A.; Planas, D.; Walsh, D.; Ponton, D. E. Cumulative effects of watershed disturbances and run-of-river dams on mercury cycling: case study and recommendations for environmental managers. *Environmental Management* **2024**. DOI: 10.1007/s00267-024-01990-6.

(76) Calder, R. S. D.; Schartup, A. T.; Li, M.; Valberg, A. P.; Balcom, P. H.; Sunderland, E. M. Future Impacts of Hydroelectric Power Development on Methylmercury Exposures of Canadian Indigenous Communities. *Environmental Science & Technology* **2016**, *50* (23), 13115-13122. DOI: 10.1021/acs.est.6b04447.

(77) Che, X.; Liu, M.; Sun, X.; Chen, J.; Ding, Y.; Fan, D. Transport of particulate mercury along the reservoir- downstream - estuary continuum during the water-sediment regulation scheme period of Yellow River in 2018. *Journal of Hazardous Materials* **2025**, *485*. DOI: 10.1016/j.jhazmat.2024.136916.

Supporting Information for

Tracing mercury from land to river: global sources, retention, and implications for sustainability

Dong Peng[1,2], Zeli Tan[3], Peipei Wu[4], Ruirong Chang[2], Shaojian Huang[2], Peng Zhang[2], Yujuan Wang[2], Zhengcheng Song[2], Yanxu Zhang[5*], Ting Lei[6], Maodian Liu[7], Beth A Middleton[8], Jianhua Gao[1], Junguo Liu[9], Guangchun Lei[6], Shu Tao[7,10]

[1]*School of Geography and Ocean Science, Ministry of Education Key Laboratory for Coast and Island Development, Nanjing University, Nanjing, China*
[2]*School of Atmospheric Sciences, Nanjing University, Nanjing, China*
[3]*Pacific Northwest National Laboratory, Richland, WA, USA*
[4]*Scripps Institution of Oceanography, University of California San Diego, La Jolla, CA, USA*
[5]*Department of Earth and Environmental Sciences, Tulane University, New Orleans, LA, USA*
[6]*School of Ecology and Nature Conservation, Beijing Forestry University, Beijing, China*
[7]*College of Urban and Environmental Sciences, Peking University, Beijing, China*
[8] *U.S. Geological Survey, Wetland and Aquatic Research Center, Lafayette, LA, USA*
[9]*Henan Provincial Key Laboratory of Hydrosphere and Watershed Water Security, North China University of Water Resources and Electric Power, Zhengzhou, China*
[10]*School of Environmental Science and Engineering, Southern University of Science and Technology, Shenzhen, China*

*Corresponding author: Yanxu Zhang (yzhang127@tulane.edu)

The supporting information contains:

Supporting text S1 to S3
Figures S1 to S5
Tables S1
Supporting Information References
Pages S1 to S19

Supporting Text

Text S1 The calculation of uncertainties from the Hg forms in the river's process

The "proportion" of particulate-phase Hg in global rivers varies significantly due to limited mechanistic research and insufficient datasets, making it challenging to accurately represent these dynamics in global river models. Observational studies, such as the observations in Yukon River, Schuster, et al. [1] observed: "*The vast majority (90%) of Hg export is associated with particulates*" and in Mackenzie River, Leitch, et al. [2] observed: "*The majority of the total Hg flux is carried in the form of particulate Hg, which accounts for 73–87% of the annual Hg flux in the past 3 yr*". Besides, in global estimations, Liu, et al. [3] recognized: "*Most riverine Hg is transported to the ocean associated with particles* [4]" and Amos, et al. [5] expressed a similar perspective, assuming that more than 95% of THg in rivers is particulate phase: "*Limited observations available suggest that rivers are highly contaminated ([Hg(D)] = 50−400 pM* [6] *and [THg] = [Hg(D)] + [Hg(P)] > 6000 pM* [7]*). We use [Hg(D)] = 50 pM as a conservative estimate.*"

Regions with dissolved phases as the majority of the total Hg (THg) are highly likely to be confined to local scales. For example, Kocman, et al. [8] reported that: "*The relatively high share of dissolved Hg forms at these sites is attributed to mercury leaching from ore residues and calcines, desorption from the particulate phase, and complexation with different organic and inorganic ligands present in water*." Indeed, a larger dissolved proportion than the particulate phase is typically observed in rivers with very low THg concentrations (Table S1). In rivers with higher THg concentrations, the particulate phase predominantly dominates. This observation is supported by earlier experimental studies, such as Lu, et al. [9], which reported: "*After spiking with mercury, the particulate mercury rose rapidly and reached over 70% of the total mercury (in the controlled experimental ecosystems).*"

Due to the absence of a biogeochemical module in the MOSART model within the CESM2 framework, Hg form changes and their impacts on riverine Hg dynamics are not accounted for in the simulations. In this study, we assumed that riverine Hg is entirely in the particulate phase, which introduces uncertainties to the model results. To address these uncertainties in both the riverine Hg budget exported to the ocean and the estimated inventory of human-induced Hg releases to rivers, we apply the below equations.

We conceptualize the global riverine Hg system as a box model, where riverine export follows mass balance principles. In this framework, the output of riverine Hg is divided into two components: losses and exports. Particulate Hg losses are primarily attributed to dam trapping, while dissolved Hg losses may result from processes such as water use and evaporation. Consequently, the following equation is applied:

$$\mathrm{PHg}_{\mathrm{flux}} \times \left(1 - Rate_{dam\ trapping}\right) + \mathrm{DHg}_{\mathrm{flux}} \times (1 - LossRate) = \mathrm{THg}_{\mathrm{export\ flux}} \quad \text{(e.S1)}$$

Where $\mathrm{PHg}_{\mathrm{flux}}$ is the particulate phase Hg (PHg) flux in global rivers (Mg/yr), the $\mathrm{Rate}_{\mathrm{dam\ trapping}}$ is the global average dam trapping rate (%), $\mathrm{DHg}_{\mathrm{flux}}$ is the dissolved phase Hg (DHg) flux in global rivers (Mg/yr), the $\mathrm{THg}_{\mathrm{export\ flux}}$ is the total Hg flux in the global rivers' export to the ocean (Mg/yr), and the LossRate is the loss rate of $\mathrm{DHg}_{\mathrm{flux}}$ in global riverine Hg processes (%). The loss of DHg associated with water use activities, such as irrigation withdrawals, evaporation, and artificial wetland purification, is assumed to be constant at 20%. This assumption is based on water use statistics [10, 11], given the limited observational data on the mechanisms governing DHg loss.

In the box model, riverine Hg is simplified into two forms: particulate Hg and dissolved Hg. Methylmercury and other Hg species are not considered due to their relatively lower proportions. Hence, the below equations are applied:

$$\mathrm{PHg}_{\mathrm{flux}} + \mathrm{DHg}_{\mathrm{flux}} = \mathrm{THg}_{\mathrm{flux}} \tag{e.S2}$$

Where $\mathrm{THg}_{\mathrm{flux}}$ is the total Hg flux in the global rivers (Mg/yr).

$$\mathrm{THg}_{\mathrm{flux}} \times \mathrm{Prop} = \mathrm{PHg}_{\mathrm{flux}} \tag{e.S3}$$

Where the Prop is the *Proportion* of particulate phase Hg in global rivers versus total Hg (%).

Additionally, the inputs of riverine Hg are simplified into two components:

$$\mathrm{ErosionHg}_{\mathrm{flux}} + \mathrm{AnthHg}_{\mathrm{flux}} = \mathrm{THg}_{\mathrm{flux}} \tag{e.S4}$$

Where $\mathrm{ErosionHg}_{\mathrm{flux}}$ is the input erosional Hg flux of the global rivers (Mg/yr), and $\mathrm{AnthHg}_{\mathrm{flux}}$ is the input anthropogenic Hg flux of the global rivers (Mg/yr).

The Hg storage in the global reservoirs/dams is equal to the losses of the particulate phase Hg in the simplified box model:

$$\mathrm{HgStorage}_{\mathrm{flux}} = \mathrm{PHg}_{\mathrm{flux}} \times \mathrm{Rate}_{\mathrm{dam\ trapping}} / 12 \tag{e.S5}$$

Where $\mathrm{HgStorage}_{\mathrm{flux}}$ is the Hg accumulation rate in dams/reservoirs each month (Mg/mon).

To address uncertainties in the particulate phase Hg proportion in rivers, we established two scenarios: (1) 70%, based on observations from the Yangtze River and controlled experiments, representing the lower bound in global rivers, particularly in highly polluted regions; and (2) 90%, derived from summarized observation records, representing the upper bound (Table S1). Besides, the $\mathrm{ErosionHg}_{\mathrm{flux}}$ remains constant at approximately 420 Mg/yr and $\mathrm{Rate}_{\mathrm{dam\ trapping}}$ efficiency is ~48%, because those parameters are not influenced by the Hg forms (Fig. 1).

Firstly, we assume the $\mathrm{THg}_{\mathrm{export\ flux}}$ is fixed at approximately 1,000 Mg/yr. Under this condition, when the "proportion" is set to 70%, the total Hg flux ($\mathrm{THg}_{\mathrm{flux}}$) is ~1,656 Mg/yr, with the anthropogenic Hg flux ($\mathrm{AnthHg}_{\mathrm{flux}}$) at ~1,236 Mg/yr and a Hg accumulation rate of ~46 Mg/month. Increasing the "proportion" to 90% raises the $\mathrm{THg}_{\mathrm{flux}}$ to ~1,825 Mg/yr, the $\mathrm{AnthHg}_{\mathrm{flux}}$ to ~1,405 Mg/yr, and the Hg accumulation rate to ~66 Mg/month. Alternatively, if we assume the THg export flux is adjustable while maintaining the AnthHgflux at ~1,500 Mg/yr, the results differ. With a "proportion" of 70%, the THg export flux reaches ~1,160 Mg/yr, and the Hg accumulation rate is ~54 Mg/month. Increasing the "proportion" to 90% results in a THg export flux of ~1,052 Mg/yr and a Hg accumulation rate of ~69 Mg/month. These results suggest that changes in the assumed Hg form have a relatively limited impact on model simulations.

In summary, our study concentrated on the particulate phase, which simplifies the Hg chemistry in the river channel and renders the model more feasible. However, we assert that this assumption is both reasonable and practical, provided that the global riverine Hg budget is predominantly dominated by the particulate phase, particularly in more polluted rivers. The relatively lower concentrations of dissolved Hg are anticipated to have minimal impact on the estimates of Hg settling and resuspension within riverine systems, encompassing channels and dams.

Text S2 Uncertainty analysis

The MOSART-Hg-WM model has uncertainties comparable to those in previous studies using the MOSART-Hg model [12]. We adopt the same model resolution as our previous study, which focuses on the pre-industrial era [12]. We find that the model with a higher resolution (0.5°×0.5°) performs better in simulating erosion flux in single topography units than a coarser resolution (1°×1°); however, the difference can be largely mitigated by using specific scaling factors. To balance computational cost and simulation accuracy, we use a resolution of 0.9° × 1.25°. In general, the accuracy of the erosion processes and riverine sediment/Hg delivery processes are validated against observations in previous studies [13, 14]. For instance, the model has better performance in simulating global sediment yield compared to alternative models such as the RUSLE model, with a 59% (mean) lower discrepancy relative to observations [13]. Additionally, sediment fluxes in the MOSART-Hg demonstrate similar performance to the BQART model [12].

The water management component (reservoirs/dams) accounts for sediment and riverine Hg trapping effects, alongside their influences on flow processes, which is supported by empirically validated relationships between reservoir properties and river parameters [15] (refer to Methods). The theoretical basin trapping by this method agrees well with the observed values, such as the Nile (observed 100% vs. theoretical 99%, mean), Kizil Irmak (observed 98% vs. theoretical 95%, mean) and Krishna River (observed 75% vs. theoretical 70%, mean) [15]. The water management module has also been validated independently in previous studies [11, 14]. Sediment flux estimations in MOSART-Hg-WM exhibit high performance compared to previous estimations [16] (Fig. S2). A similar level of model accuracy is expected for the Hg-trapping effects of reservoirs and dams.

Another source of uncertainties is the spatial distribution of anthropogenic Hg sources to freshwater environments. We consider two different atmospheric Hg inventories, AMAP inventory [17] and Streets inventory [18], as a proxy for the spatial distribution of anthropogenic releases to rivers. The riverine Hg export fluxes from both scenarios (*AMAP scenario* and *Streets scenario* hereafter) exhibit a strong correlation with observations at a global scale (Fig. S3). However, the different spatial distributions of Hg sources result in varied performances in different regions. The *Streets scenario* has a better performance in simulating riverine Hg in North America, while the *AMAP scenario* performs better in other regions, particularly due to the more detailed sector contributions for the latter.

The soil Hg concentration datasets play a crucial role in the Hg erosion processes. The diverse datasets (Wang dataset and Liu dataset, refer to Method) exert limited impacts on global-scale riverine Hg export fluxes, with the Liu dataset resulting in only a slight increase in riverine Hg export to oceans (<10%) than using the Wang dataset. Furthermore, the *Deposition Experiment* is devised to assess uncertainties arising from the change of soil Hg concentrations due to atmospheric Hg deposition and the loss of soil Hg by erosion (Table 1). In this experiment, soil Hg concentrations are dynamically adjusted based on the atmospheric deposition and erosion processes. However, the disparities between the scenarios with constant and dynamic soil Hg concentrations are minimal, with changes in riverine Hg export to oceans < 2% (Fig. S4). Similarly, given that the rates of gaseous Hg evaporating from rivers are lower than the atmospheric Hg deposition rates [19], the combined uncertainties from gaseous Hg evaporating and deposition are expected to remain within 2%.

The transformation of Hg forms in riverine processes is not explicitly accounted for in our model, and the assumption that all Hg exists in the particulate phase leads to an overestimation of both Hg trapping in reservoirs and anthropogenic Hg releases to rivers. Directly applying empirical particulate Hg fractions is unfeasible. Our macro-scale model cannot resolve dynamic local partitioning covariates like pH or DOC, and extrapolating spatially biased observations would introduce unacceptable uncertainties. To address this uncertainty, we set up two scenarios for estimates: (1) 70% Particulate Hg: Based on observations from the Yangtze River and controlled ecosystem experiments, this scenario represents a lower bound; (2) 90% Particulate Hg: Based on observations from the Yukon River and prior estimates by Amos, et al. [5], this scenario represents an upper bound.

The results show that under the 70% and 90% particulate-phase scenarios, anthropogenic Hg releases are approximately 1,236 Mg/yr (mean) and 1,405 Mg/yr (mean), respectively, assuming a riverine Hg export of ~1,000 Mg/yr (mean) to oceans. Our estimated range of anthropogenic Hg releases (1,100–2,000 Mg/yr) effectively captures these uncertainties. The corresponding trapped Hg pools in reservoirs and dams are ~552 Mg/yr (mean) and ~792 Mg/yr (mean), respectively, which are lower than the ~900 Mg/yr (mean) estimated under the 100% particulate-phase assumption. Additionally, if anthropogenic Hg releases are held constant at ~1,500 Mg/yr, the riverine Hg export fluxes to oceans under the 70% and 90% particulate-phase scenarios are ~1,160 Mg/yr (mean) and ~1,052 Mg/yr (mean), respectively. Overall, the uncertainties arising from changes in Hg forms in our simulations have a limited impact on the global riverine Hg transport and export flux. Furthermore, the proportion of particulate-phase Hg in global rivers varies and is influenced by factors such as organic carbon content and pH [20]. Thus, incorporating biogeochemical cycling within an Earth system model can help improve riverine Hg estimates, however, which is currently absent in our approach. Details of these calculations are provided in Text S1.

Text S3 Implications for Hg cycling and sustainable science

Our assessments emphasize the role of dams/reservoirs as the sink in global Hg biogeochemistry. The accumulation of Hg in global reservoirs adds complexity to environmental governance efforts. In the short term, Hg pools increase through particulate sedimentation, while transformations such as changes in Hg speciation and bioavailability can reduce the mobile fraction. Despite high Hg levels, reservoir trapping efficiency remains largely unaffected, as it is driven primarily by sediment accumulation rather than Hg content. Over the long term in some reservoirs, Hg buried in deeper sediment layers, with limited exchange with bottom waters and have no possibility to be resuspended, can be considered effectively sequestered, particularly in deeper or smaller reservoirs, provided dredging does not occur. Management actions such as dredging can help remove sediment-bound Hg from the riverbed, reducing its potential remobilization into the aquatic system. The settled Hg in reservoirs creates a suitable environment for Hg methylation [21], with conditions similar to those of nutrient-rich wetlands that support biological activity and methylation.

Our findings provide insights into the size and behavior of Hg pools in global reservoirs, which can be used to assess methylation risks for human health and inform future monitoring efforts. Hg pollution has long been recognized as a sustainability challenge [22], particularly because riverine Hg contamination poses direct threats to multiple the United Nations Sustainable Development Goals (SDGs) (https://www.undp.org/sustainable-development-goals)—notably SDG 3 (Good Health and Well-being) and SDG 6 (Clean Water and Sanitation). While water infrastructure supports agriculture, hydropower, and flood control, Hg accumulated in reservoir sediments and riverbeds can serve as secondary sources of contamination [23, 24], posing risks to both food and water security. For example, observations from the Yangtze River suggest that Hg retained in the Three Gorges Reservoir has become a downstream source of riverine Hg due to declining upstream Hg inputs [24]. Watershed management practices, such as dam construction, hydroelectric development, and water-sediment regulation, can significantly influence Hg fluxes and deposition patterns. Hydropower reservoirs may create conditions conducive to methylation [25], leading to elevated methylmercury concentrations in rivers, estuaries, and aquatic organisms [26]; while sediment flushing operations alter the downstream transport and fate of particulate-bound Hg [27].

Our model provides a process-based, spatially explicit scientific framework for assessing and managing the risks associated with Hg pollution in river systems. It supports the development of targeted mitigation strategies to reduce human exposure and promote more sustainable water infrastructure planning. In particular, our global estimates of Hg accumulation in reservoirs can inform environmental restoration efforts, enhance monitoring under international frameworks such as the Minamata Convention on Mercury, and contribute to SDG 17 (Partnerships for the Goals) (https://www.undp.org/sustainable-development-goals) by facilitating data-driven collaboration across regions. This work also offers a science-based foundation for risk assessments related to dam operation, modification, and removal, supporting integrated watershed and infrastructure management.

Figures

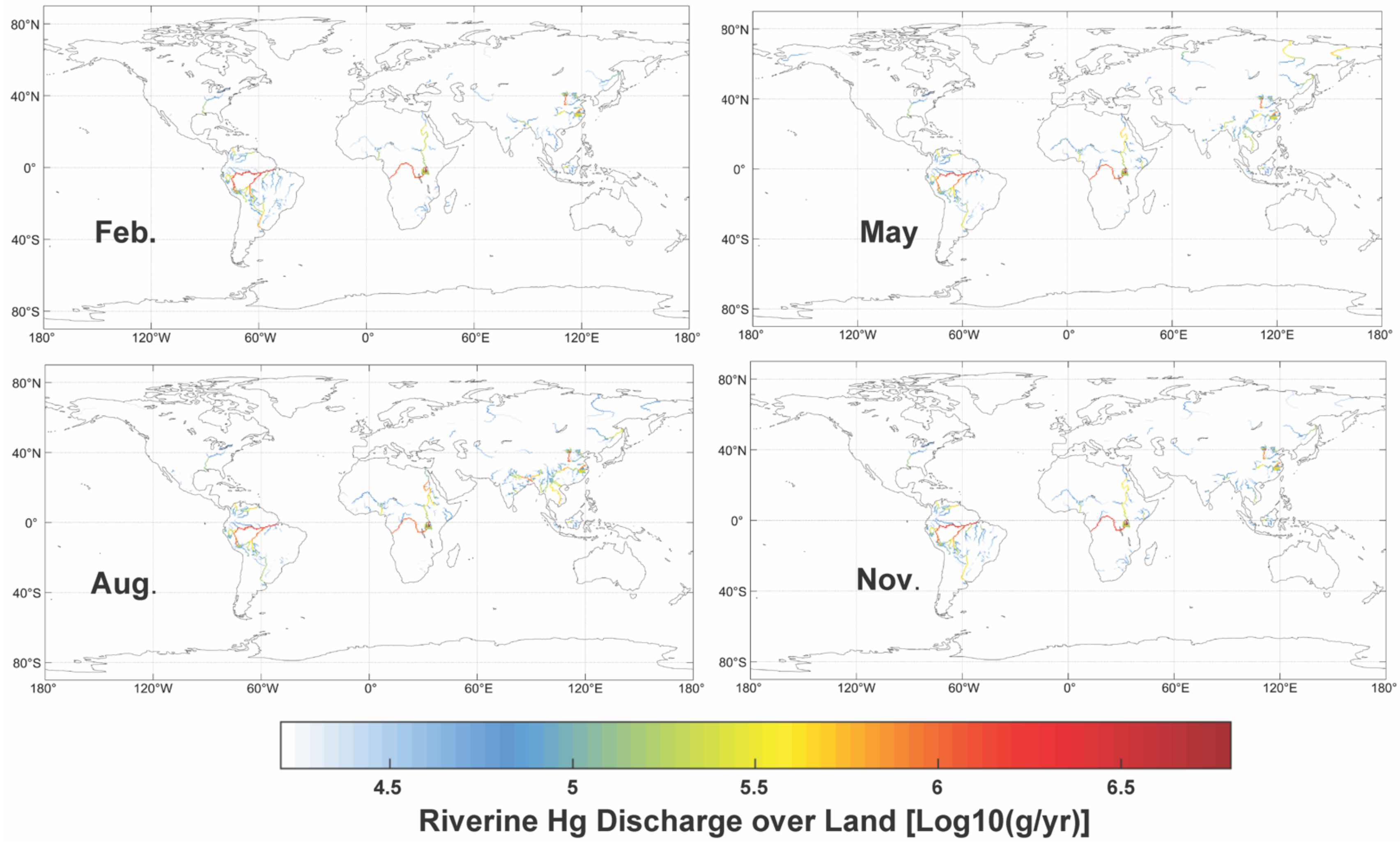

Figure S1 Seasonal fluxes of riverine mercury discharge over land

Figure S2 The sediment load of estimation versus other estimations [16]. The 1950/2010 sediment load is referred to as the estimation by Syvitski, et al. [16].

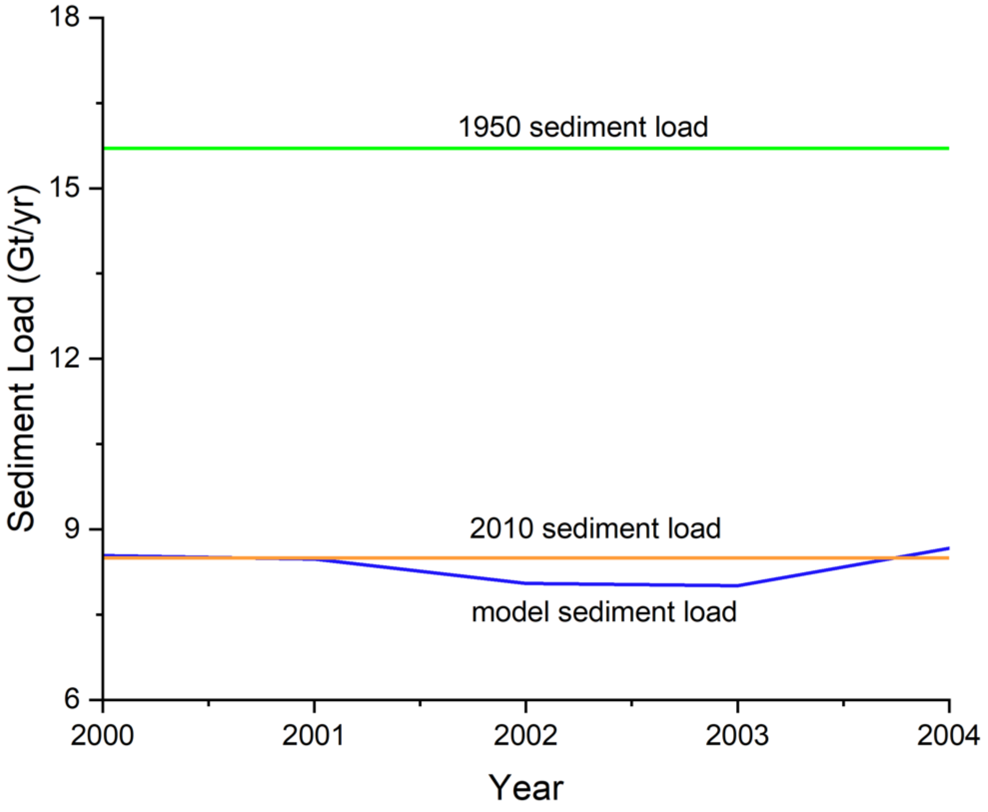

Figure S3 The comparison of modeled riverine Hg fluxes export by rivers under Inventory Experiment with observation, AMAP represents the AMAP inventory, the Streets represent the Streets inventory (refer to Table 1). Unit kg/yr.

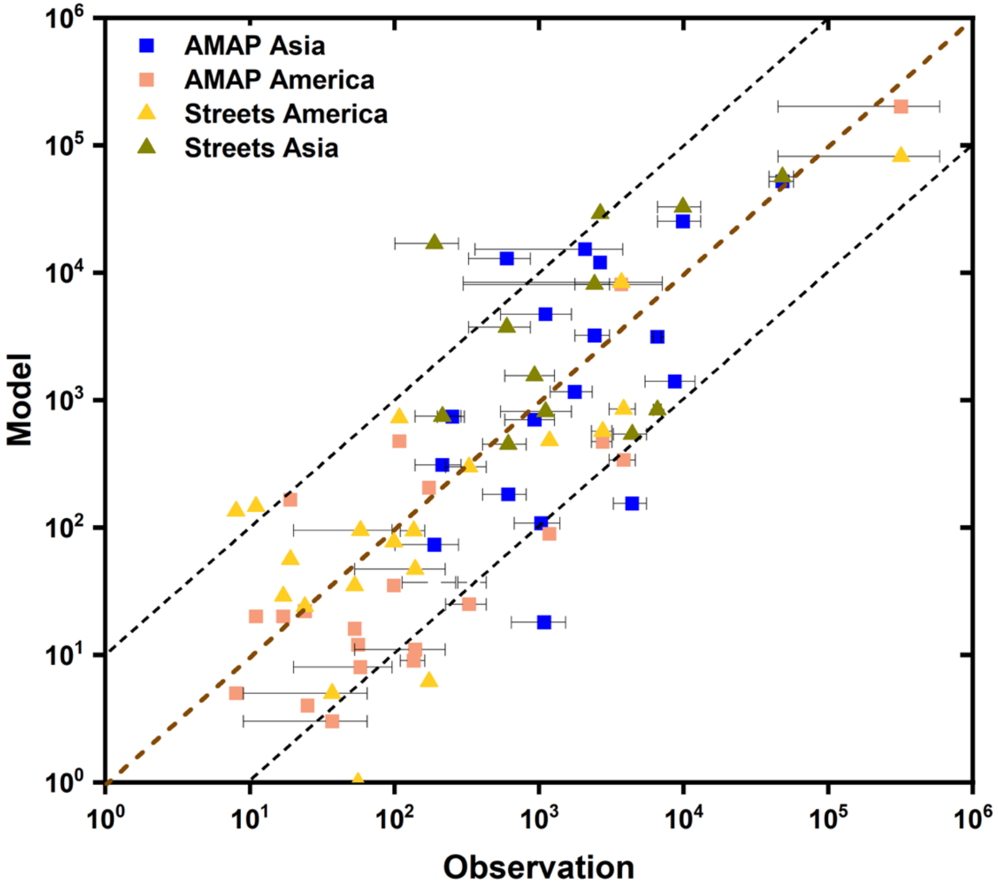

Figure S4 The comparison of Model results by ***Soil Hg Experiment*** with observation, Wang represents the soil Hg concentration of Wang, et al. [28], the Chen represents the soil Hg concentration dataset of Liu, et al. [29] (refer to Table 1).

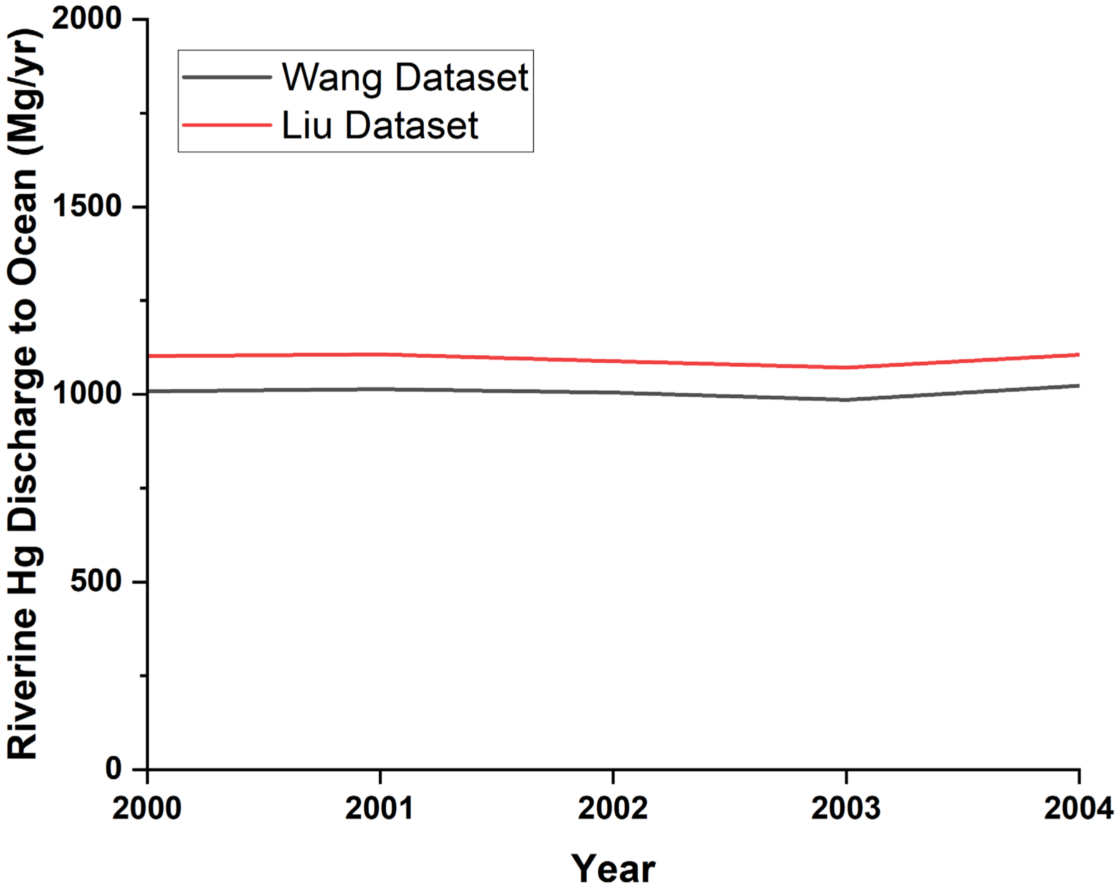

Figure S5 The comparison of Model results by ***Deposition Experiment*****,** the Deposition represents the condition with dynamic soil Hg and atmospheric Hg deposition in **Table 1**, and the Without Deposition represents the condition with fixed soil Hg concentration in **Table 1**.

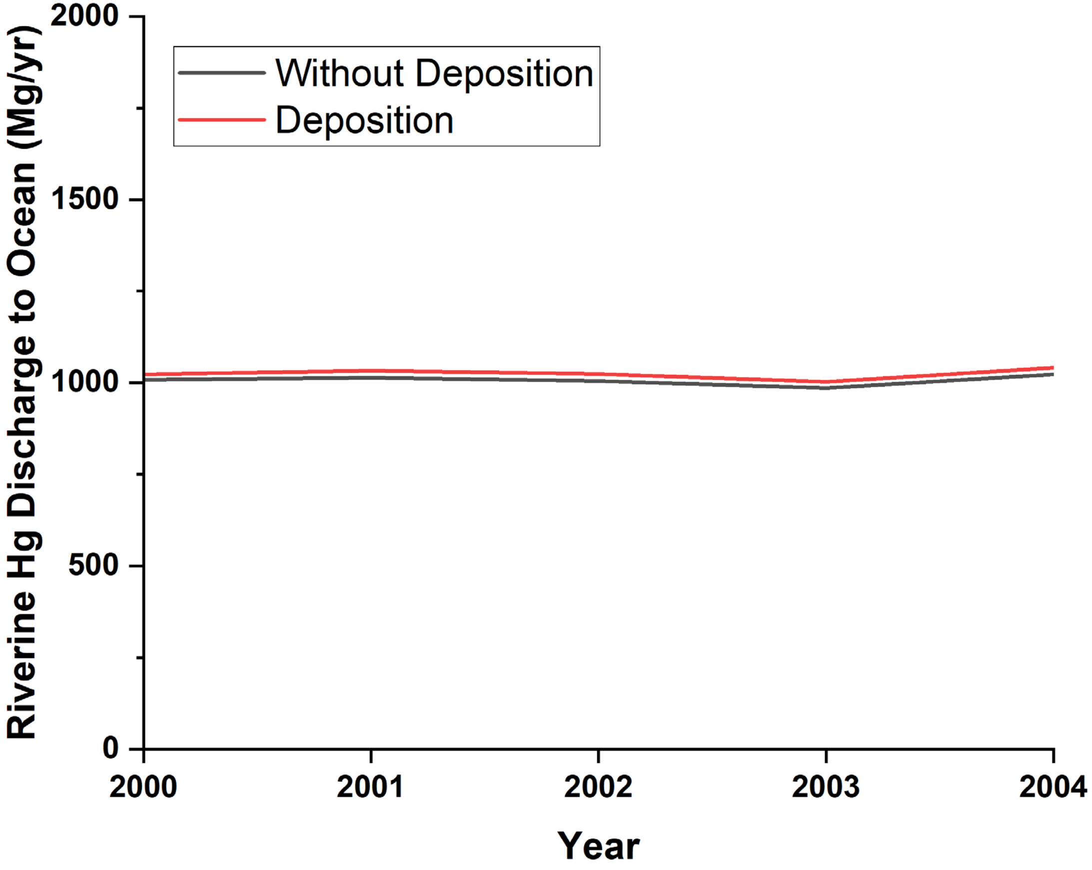

Tables

Table S1 Hg Forms in Global Rivers and the Proportion of Particulate Phase Hg Relative to Total Hg (Parts of the records are summary based on Supplementary Table 1 in Liu, et al. [3])

River/Place Name	Region	Total Hg concentration, ng/L	Particulate Hg concentration, ng/L	Dissolved Hg concentration, ng/L	Proportion of particulate Hg/total Hg, %	References
Amazon's main tributaries (rising water stage)	Americas	5	2	3	40%	20
Amazon's main tributaries (dry season)		4.2	1	3.2	24%	
Amazon main tributaries (rising water stage)		28.2	25.6	2.6	91%	
Amazon main tributaries (flood peak)		18.8	17	1.8	90%	
Amazon's main tributaries (dry season)		10	7.8	2.2	78%	
Amazon main tributaries (rising water stage)		37.1	33.1	4	89%	
Amazon main tributaries (flood peak)		14.6	11.8	2.8	81%	
Amazon's main tributaries (dry season)		7.4	5.6	1.8	76%	
Amazon River (rising water stage)		19.1	15.7	3.4	82%	
Amazon River (flood peak)		6.4	1.8	4.6	28%	
Amazon River (dry season)		33.4	31	2.4	93%	
Marano Lagoon (Italy)	Europe	44	32	13	73%	30
Austria Sites		0.37	0.16	0.21	43%	31
Austria Sites		0.57	0.39	0.18	68%	
Austria Sites		0.95	0.13	0.82	14%	
Bei River (China)	Asia	5.6	4.6	1	82%	3
Bei River (China)		8.4	6.5	1.9	77%	
Bei River (China)		9.9	8.7	1.2	88%	

Bei River (China)		12	10	1.6	83%	
Berry Creek Estuary	Americas	280	240	40	86%	32
Bulgaria Sites	Europe	0.26	0.02	0.24	8%	31
Bulgaria Sites		0.28	0.07	0.21	25%	
Churchill	Americas	2	0.3	1.7	15%	1
Churchill		2	0.3	1.7	15%	33
Churchill		3.5	0.2	3.3	6%	34
Connecticut		2.2	0.96	1.2	44%	35
Connecticut		2.2	1.5	0.75	68%	
Connecticut		2.4	0.81	1.6	34%	
Connecticut		2.8	1.1	1.8	39%	
Connecticut		3.2	1.6	1.6	50%	
Connecticut		3.4	1.5	1.9	44%	
Connecticut		3.5	2.5	0.97	71%	
Connecticut		4.3	0.96	3.4	22%	
Connecticut		4.4	2.7	1.7	61%	
Connecticut		4.7	4	0.73	85%	
Connecticut		4.9	1.8	3.1	37%	
Connecticut		5	3.1	2	62%	
Connecticut		5.3	1.9	3.4	36%	
Connecticut		9.3	6	3.3	65%	
Corno	Europe	40	16	24	40%	30
Dong River (China)	Asia	6.1	3.7	2.4	61%	3
Dong River (China)		6.1	4.3	1.8	70%	
Dong River (China)		9.2	6.6	2.6	72%	
Dong River (China)		12	10	1.8	83%	
East River (China)		17	5.9	12	35%	36
East River (China)		17	8	9	47%	

East River (China)		17	11	6.3	65%	
East River (China)		18	5.5	13	31%	
East River (China)		19	8.3	11	44%	
East River (China)		19	11	7.9	58%	
East River (China)		21	6.9	14	33%	
East River (China)		24	8	16	33%	
East River (China)		24	8.2	15	34%	
France Sites	Europe	0.51	0.03	0.48	6%	31
France Sites		0.88	0.47	0.41	53%	
Garonne River La Réole		11	9.9	0.6	90%	37
Garonne River La Réole		15	14	1.2	93%	
Garonne River La Réole		19	18	0.9	95%	
Garonne River La Réole		23	22	0.7	96%	
Garonne River La Réole		40	39	1	98%	
Garonne River P.-Ste-Marie		8	7.3	0.7	91%	
Garonne River P.-Ste-Marie		12	11	1.2	92%	
Garonne River P.-Ste-Marie		14	13	0.9	93%	
Great Whale River	Americas	2.8	0.6	2.2	21%	34
Great Britain Sites	Europe	0.28	0.12	0.16	43%	31
Great Britain Sites		0.42	0.18	0.24	43%	
Great Britain Sites		2.8	0.48	2.3	17%	
Guandu River	Americas	220	190	35	86%	38
Guarda River		20	19	0.5	95%	
Hackensack River		16	14	2.1	88%	32
Han River	Asia	14	4.3	10	31%	3
Han River		23	5.7	18	25%	
Huai River		53	43	10	81%	39
Huangpu River		15	11	4.3	73%	3

Huangpu River		160	150	4.5	94%	
Hudson River	Americas	13	12	0.62	92%	40
Ita River		1.6	0.27	1.4	17%	38
Itimirim River		1	0.4	0.4	40%	
Itinguçu River		2.4	1.2	1.2	50%	
Jin River (China)	Asia	7	3.8	3.2	54%	3
Jin River (China)		8	4.6	3.4	58%	
Jiulong River (China)		8.6	4.5	4.1	52%	
Jiulong River (China)		10	6.3	3.8	63%	
Lena River		1.7	1	0.7	59%	41
Lena River		1.8	1.1	0.64	61%	
Lena River		1.9	0.86	1.1	45%	
Lena River		1.9	1.3	0.6	68%	
Lena River		2.6	1.6	1	62%	41; 1
Lena River		2.9	2.4	0.5	83%	41
Lena River		4.8	3.9	0.9	81%	
Liao River		11	7.8	3.5	71%	3
Liao River		12	8.6	3.3	72%	
Liao River		13	11	2.2	85%	
Liao River		14	10	4.4	71%	
Luan River		12	8.4	3.8	70%	
Luan River		13	9.1	3.7	70%	
Mackenzie River	Americas	7	4.2	2.8	60%	2
Mackenzie River		15	13	1.6	87%	42
Maderia River		9.5	3.9	5.5	41%	43
Major tributaries flowing into the Gulf of Maine		4.4	2.2	2.2	50%	44
Mekong River	Asia	0.92	0.52	0.4	57%	45
Mekong River		0.92	0.68	0.24	74%	

Mekong River		0.94	0.7	0.24	74%	
Mekong River		1.5	1.2	0.32	80%	
Mekong River		2.2	1.3	0.88	59%	
Mekong River		2.4	1.5	0.9	63%	
Mekong River		2.4	1.8	0.62	75%	
Mekong River		3.4	2.3	1.1	68%	
Mekong River		5.2	4.6	0.62	88%	
Mekong River		6.4	5.4	0.96	84%	
Mekong River		6.8	5.2	1.6	76%	
Mekong River		7.8	6.5	1.3	83%	
Mekong River		9	7.4	1.6	82%	
Mekong River		11	8	2.8	73%	
Mekong River		11	10	0.56	91%	
Mekong River		16	14	2	88%	
Min River		10	7	3.3	70%	3
Min River		11	8.1	3	74%	
Min River		12	7.1	4.9	59%	
Min River		17	10	6.8	59%	
Mississippi River	Americas	5.8	4.7	1.1	81%	1
Nandu River	Asia	8.5	4.6	3.8	54%	3
Nandu River		11	6.5	4.2	59%	
Negro River	Americas	12	5.6	6	47%	43
Negro River		18	11	7.1	61%	
Nelson River		0.88	0.38	0.5	43%	33
Nelson River		0.9	0.4	0.5	44%	1
Nelson River		2.2	0.3	1.9	14%	34
New York/New Jersey Harbor Estuary		17	16	0.62	94%	40
Nile River	Asia	2.2	1.8	0.36	82%	46

Ob' River		0.56	0.14	0.42	25%	[41]
Ob' River		0.62	0.22	0.4	35%	
Ob' River		0.84	0.26	0.58	31%	
Ob' River		0.97	0.21	0.76	22%	
Ob' River		1.1	0.52	0.62	47%	
Ob' River		1.2	0.58	0.58	48%	
Ob' River		1.3	0.65	0.62	50%	
Ob' River		1.7	1.1	0.6	65%	[41]; [1]
Ob' River		2.5	2	0.48	80%	[41]
Ob' River		7.4	6.8	0.64	92%	
Ou River		10	6.4	3.7	64%	[3]
Ou River		14	11	3.4	79%	
Peel River	Americas	22	20	2	91%	[42]
Qiantang River	Asia	8.9	6.7	2.2	75%	[3]
Qiantang River		12	8.4	3.8	70%	
Qiantang River		16	12	4.2	75%	
Qiantang River		19	15	4.1	79%	
Rhône River	Europe	6	4.9	1.1	82%	[46]
San Francisco Estuary	Americas	6	4.8	1.2	80%	[47]
San Francisco Estuary		6.6	5.2	1.4	79%	[48]
São Francisco River		37	37	0.25	100%	[38]
Sinnamary estuary		22	21	1.2	95%	[49]
Solimoes		7.2	1.9	5.3	26%	[43]
Solimoes		9.2	3	6.2	33%	
Solimoes		11	5.9	5.5	54%	
Solimoes		14	7	6.9	50%	
Spain Sites	Europe	0.37	0.09	0.28	24%	[31]
Spain Sites		0.46	0.09	0.37	20%	

Spain Sites		0.94	0.36	0.58	38%	
St. Lawrence River	Americas	2.8	2.2	0.6	79%	1
Sweden Sites	Europe	0.18	0.02	0.16	11%	31
Sweden Sites		0.86	0.25	0.61	29%	
Xi River	Asia	4.5	3.4	1.2	76%	3
Xi River		6	2.4	3.6	40%	
Xi River		11	7.9	2.6	72%	
Xi River		24	20	4.2	83%	
Yalu River		10	6.8	3.5	68%	
Yalu River		14	11	3.2	79%	
Yalu River		57	37	20	65%	50
Yangtze River		35	24	11	69%	51
Yangtze River		17	11	5.8	65%	23
Yangtze River		19	8.2	11	43%	
Yangtze River		19	13	6.5	68%	
Yangtze River		20	12	7.9	60%	
Yangtze River		22	8.7	14	40%	
Yangtze River		22	9.9	12	45%	
Yangtze River		25	12	13	48%	
Yangtze River		29	17	11	59%	
Yangtze River		30	18	11	60%	
Yangtze River		33	19	14	58%	
Yangtze River		34	16	18	47%	
Yangtze River		39	20	19	51%	
Yangtze River		93	69	24	74%	
Yellow River		19	17	1.9	89%	3
Yellow River		25	21	4	84%	
Yellow River		27	20	6.4	74%	

Yellow River		29	25	3.9	86%	
Yenisei River		0.35	0.19	0.16	54%	41
Yenisei River		0.35	0.21	0.14	60%	
Yenisei River		0.45	0.29	0.16	64%	
Yenisei River		0.51	0.31	0.2	61%	
Yenisei River		0.58	0.24	0.34	41%	
Yenisei River		0.7	0.28	0.42	40%	
Yenisei River		0.71	0.27	0.44	38%	
Yenisei River		0.8	0.5	0.3	63%	1, 41
Yenisei River		0.82	0.14	0.68	17%	41
Yenisei River		0.82	0.54	0.28	66%	
Yenisei River		0.95	0.39	0.56	41%	
Yenisei River		0.96	0.72	0.24	75%	
Yenisei River		1.5	1.2	0.3	80%	
Yenisei River		2.7	1.8	0.88	67%	
Yukon River	Americas	15	13	1.9	87%	1

References

(1) Schuster, P. F.; Striegl, R. G.; Aiken, G. R.; Krabbenhoft, D. P.; Dewild, J. F.; Butler, K.; Kamark, B.; Dornblaser, M. Mercury export from the Yukon River Basin and potential response to a changing climate. *Environmental Science & Technology* **2011**, *45* (21), 9262-9267. DOI: 10.1021/es202068b.

(2) Leitch, D. R.; Carrie, J.; Lean, D.; Macdonald, R. W.; Stern, G. A.; Wang, F. The delivery of mercury to the Beaufort Sea of the Arctic Ocean by the Mackenzie River. *Science of The Total Environment* **2007**, *373* (1), 178-195. DOI: 10.1016/j.scitotenv.2006.10.041.

(3) Liu, M.; Zhang, Q.; Maavara, T.; Liu, S.; Wang, X.; Raymond, P. A. Rivers as the largest source of mercury to coastal oceans worldwide. *Nature Geoscience* **2021**, *14* (9), 672-677. DOI: 10.1038/s41561-021-00793-2.

(4) Sonke, J. E.; Teisserenc, R.; Heimbürger-Boavida, L.-E.; Petrova, M. V.; Marusczak, N.; Le Dantec, T.; Chupakov, A. V.; Li, C.; Thackray, C. P.; Sunderland, E. M.; et al. Eurasian river spring flood observations support net Arctic Ocean mercury export to the atmosphere and Atlantic Ocean. *Proceedings of the National Academy of Sciences* **2018**, *115* (50). DOI: 10.1073/pnas.1811957115.

(5) Amos, H. M.; Jacob, D. J.; Kocman, D.; Horowitz, H. M.; Zhang, Y.; Dutkiewicz, S.; Horvat, M.; Corbitt, E. S.; Krabbenhoft, D. P.; Sunderland, E. M. Global biogeochemical implications of mercury discharges from rivers and sediment burial. *Environmental Science and Technology* **2014**, *48* (16), 9514-9522. DOI: 10.1021/es502134t.

(6) Ram, A.; Rokade, M. A.; Borole, D. V.; Zingde, M. D. Mercury in sediments of Ulhas estuary. *Marine Pollution Bulletin* **2003**, *46* (7), 846-857. DOI: 10.1016/s0025-326x(03)00065-1.

(7) Sankar, R.; Ramkumar, L.; Rajkumar, M.; Sun, J.; Ananthan, G. Seasonal variations in physico-chemical parameters and heavy metals in water and sediments of Uppanar estuary, Nagapattinam, India. *J Environ Biol* **2010**, *31* (5), 681-686.

(8) Kocman, D.; Kanduč, T.; Ogrinc, N.; Horvat, M. Distribution and partitioning of mercury in a river catchment impacted by former mercury mining activity. *Biogeochemistry* **2010**, *104* (1-3), 183-201. DOI: 10.1007/s10533-010-9495-5.

(9) Lu, X.; Johnson, K. W.; Whitney, F. A.; Wong, C. S.; Wu, J. A study on the flux, speciation, and budget of mercury in controlled experimental ecosystems. *Chinese Journal of Oceanology and Limnology* **1987**, *5* (2), 146-160. DOI: 10.1007/bf02844999.

(10) McDermid, S.; Nocco, M.; Lawston-Parker, P.; Keune, J.; Pokhrel, Y.; Jain, M.; Jägermeyr, J.; Brocca, L.; Massari, C.; Jones, A. D.; et al. Irrigation in the Earth system. *Nature Reviews Earth & Environment* **2023**, *4* (7), 435-453. DOI: 10.1038/s43017-023-00438-5.

(11) Zhou, T.; Leung, L. R.; Leng, G.; Voisin, N.; Li, H. Y.; Craig, A. P.; Tesfa, T.; Mao, Y. Global irrigation characteristics and effects simulated by fully coupled land surface, river, and water management models in E3SM. *J Adv Model Earth Sy* **2020**, *12* (10). DOI: 10.1029/2020ms002069.

(12) Peng, D.; Tan, Z.; Yuan, T.; Wu, P.; Song, Z.; Zhang, P.; Huang, S.; Zhang, Y.; Lei, T.; Middleton, B. A.; et al. Human perturbations to mercury in global rivers. *Sci Adv* **2025**, *11* (24), eadw0471. DOI: 10.1126/sciadv.adw0471 From NLM Medline.

(13) Tan, Z. L.; Leung, L. R.; Li, H. Y.; Tesfa, T. Modeling sediment yield in land surface and earth system models: model comparison, development, and evaluation. *J Adv Model Earth Sy* **2018**, *10* (9), 2192-2213, Article. DOI: 10.1029/2017ms001270.

(14) Li, H.-Y.; Tan, Z.; Ma, H.; Zhu, Z.; Abeshu, G. W.; Zhu, S.; Cohen, S.; Zhou, T.; Xu, D.; Leung, L. R. A new large-scale suspended sediment model and its application over the United States. *Hydrology and Earth System Sciences* **2022**, *26* (3), 665-688. DOI: 10.5194/hess-26-665-2022.

(15) Vörösmarty, C. J.; Meybeck, M.; Fekete, B.; Sharma, K.; Green, P.; Syvitski, J. P. M. Anthropogenic sediment

retention: major global impact from registered river impoundments. *Global and Planetary Change* **2003**, *39* (1-2), 169-190. DOI: 10.1016/s0921-8181(03)00023-7.

(16) Syvitski, J.; Ángel, J. R.; Saito, Y.; Overeem, I.; Vörösmarty, C. J.; Wang, H.; Olago, D. Earth's sediment cycle during the Anthropocene. *Nature Reviews Earth & Environment* **2022**, *3* (3), 179-196. DOI: 10.1038/s43017-021-00253-w.

(17) Steenhuisen, F.; Wilson, S. J. Geospatially distributed (gridded) global mercury emissions to air from anthropogenic sources in 2015. *DataverseNL* **2022**. DOI: doi:10.34894/SZ2KOI. Steenhuisen, F.; Wilson, S. J. Development and application of an updated geospatial distribution model for gridding 2015 global mercury emissions. *Atmos. Environ.* **2019**, *211*, 138-150. DOI: 10.1016/j.atmosenv.2019.05.003.

(18) Streets, D. G.; Horowitz, H. M.; Lu, Z.; Levin, L.; Thackray, C. P.; Sunderland, E. M. Global and regional trends in mercury emissions and concentrations, 2010–2015. *Atmos. Environ.* **2019**, *201*, 417-427. DOI: 10.1016/j.atmosenv.2018.12.031.

(19) da Silva, G. S.; Jardim, W. F.; Fadini, P. S. Elemental gaseous mercury flux at the water/air interface over the Negro River basin, Amazon, Brazil. *Science of The Total Environment* **2006**, *368* (1), 189-198. DOI: 10.1016/j.scitotenv.2005.09.082.

(20) Maia, P. D.; Maurice, L.; Tessier, E.; Amouroux, D.; Cossa, D.; Pérez, M.; Moreira-Turcq, P.; Rhéault, I. Mercury distribution and exchanges between the Amazon River and connected floodplain lakes. *Science of The Total Environment* **2009**, *407* (23), 6073-6084. DOI: 10.1016/j.scitotenv.2009.08.015.

(21) Hsu-Kim, H.; Eckley, C. S.; Achá, D.; Feng, X.; Gilmour, C. C.; Jonsson, S.; Mitchell, C. P. J. Challenges and opportunities for managing aquatic mercury pollution in altered landscapes. *Ambio* **2018**, *47* (2), 141-169. DOI: 10.1007/s13280-017-1006-7. Ma, H.; Chen, Q.; Liu, D.; Chen, Y.; Lin, Y.; Zhang, J.; Yan, X. Impacts of river damming on sediment methylmercury dynamics. *ACS ES&T Water* **2023**, *3* (4), 934-942. DOI: 10.1021/acsestwater.2c00397. Pestana, I. A.; Azevedo, L. S.; Bastos, W. R.; Magalhães de Souza, C. M. The impact of hydroelectric dams on mercury dynamics in South America: A review. *Chemosphere* **2019**, *219*, 546-556. DOI: 10.1016/j.chemosphere.2018.12.035.

(22) Sodeno, R. Analysis of the Minamata Convention on Mercury in the Context of Sustainable Development Goals (SDGs). *Global Environmental Research* **2020**, 065-070. Selin, H.; Selin, N. E. From Stockholm to Minamata and beyond: Governing mercury pollution for a more sustainable future. *One Earth* **2022**, *5* (10), 1109-1125. DOI: 10.1016/j.oneear.2022.09.001.

(23) Liu, M.; He, Y.; Baumann, Z.; Zhang, Q.; Jing, X.; Mason, R. P.; Xie, H.; Shen, H.; Chen, L.; Zhang, W.; et al. The impact of the Three Gorges Dam on the fate of metal contaminants across the river-ocean continuum. *Water Research* **2020**, *185*, 116295. DOI: 10.1016/j.watres.2020.116295.

(24) Peng, D.; Lyu, J.; Song, Z.; Huang, S.; Zhang, P.; Gao, J.; Zhang, Y. Mercury budgets in the suspended particulate matters of the Yangtze River. *Water Research* **2023**, *243*. DOI: 10.1016/j.watres.2023.120390.

(25) Amyot, M.; Bilodeau, F.; Tremblay, A.; Planas, D.; Walsh, D.; Ponton, D. E. Cumulative effects of watershed disturbances and run-of-river dams on mercury cycling: case study and recommendations for environmental managers. *Environmental Management* **2024**. DOI: 10.1007/s00267-024-01990-6.

(26) Calder, R. S. D.; Schartup, A. T.; Li, M.; Valberg, A. P.; Balcom, P. H.; Sunderland, E. M. Future Impacts of Hydroelectric Power Development on Methylmercury Exposures of Canadian Indigenous Communities. *Environmental Science & Technology* **2016**, *50* (23), 13115-13122. DOI: 10.1021/acs.est.6b04447.

(27) Che, X.; Liu, M.; Sun, X.; Chen, J.; Ding, Y.; Fan, D. Transport of particulate mercury along the reservoir-downstream - estuary continuum during the water-sediment regulation scheme period of Yellow River in 2018. *Journal of Hazardous Materials* **2025**, *485*. DOI: 10.1016/j.jhazmat.2024.136916.

(28) Wang, X.; Yuan, W.; Lin, C.-J.; Zhang, L.; Zhang, H.; Feng, X. Climate and vegetation as primary drivers for

global mercury storage in surface soil. *Environmental Science & Technology* **2019**, *53* (18), 10665-10675. DOI: 10.1021/acs.est.9b02386.

(29) Liu, Y.-R.; Guo, L.; Yang, Z.; Xu, Z.; Zhao, J.; Wen, S.-H.; Delgado-Baquerizo, M.; Chen, L. Multidimensional drivers of mercury distribution in global surface soils: insights from a global standardized field survey. *Environmental Science & Technology* **2023**, *57* (33), 12442-12452. DOI: 10.1021/acs.est.3c04313.

(30) Covelli, S.; Acquavita, A.; Piani, R.; Predonzani, S.; De Vittor, C. Recent contamination of mercury in an estuarine environment (Marano lagoon, Northern Adriatic, Italy). *Estuarine, Coastal and Shelf Science* **2009**, *82* (2), 273-284. DOI: 10.1016/j.ecss.2009.01.021.

(31) Bravo, A. G.; Kothawala, D. N.; Attermeyer, K.; Tessier, E.; Bodmer, P.; Ledesma, J. L. J.; Audet, J.; Casas-Ruiz, J. P.; Catalán, N.; Cauvy-Fraunié, S.; et al. The interplay between total mercury, methylmercury and dissolved organic matter in fluvial systems: A latitudinal study across Europe. *Water Research* **2018**, *144*, 172-182. DOI: 10.1016/j.watres.2018.06.064.

(32) Cardona-Marek, T.; Schaefer, J.; Ellickson, K.; Barkay, T.; Reinfelder, J. R. Mercury Speciation, Reactivity, and Bioavailability in a Highly Contaminated Estuary, Berry's Creek, New Jersey Meadowlands. *Environmental Science & Technology* **2007**, *41* (24), 8268-8274. DOI: 10.1021/es070945h.

(33) Kirk, J. L.; St. Louis, V. L.; Hintelmann, H.; Lehnherr, I.; Else, B.; Poissant, L. Methylated Mercury Species in Marine Waters of the Canadian High and Sub Arctic. *Environmental Science & Technology* **2008**, *42* (22), 8367-8373. DOI: 10.1021/es801635m.

(34) Hare, A.; Stern, G. A.; Macdonald, R. W.; Kuzyk, Z. Z.; Wang, F. Contemporary and preindustrial mass budgets of mercury in the Hudson Bay Marine System: The role of sediment recycling. *Science of The Total Environment* **2008**, *406* (1-2), 190-204. DOI: 10.1016/j.scitotenv.2008.07.033.

(35) Balcom, P. H.; Fitzgerald, W. F.; Vandal, G. M.; Lamborg, C. H.; Rolfhus, K. R.; Langer, C. S.; Hammerschmidt, C. R. Mercury sources and cycling in the Connecticut River and Long Island Sound. *Marine Chemistry* **2004**, *90* (1-4), 53-74. DOI: 10.1016/j.marchem.2004.02.020.

(36) Liu, J.; Feng, X.; Zhu, W.; Zhang, X.; Yin, R. Spatial distribution and speciation of mercury and methyl mercury in the surface water of East River (Dongjiang) tributary of Pearl River Delta, South China. *Environ. Sci. Pollut. Res.* **2011**, *19* (1), 105-112. DOI: 10.1007/s11356-011-0542-0.

(37) Schäfer, J.; Blanc, G.; Audry, S.; Cossa, D.; Bossy, C. Mercury in the Lot–Garonne River system (France): Sources, fluxes and anthropogenic component. *Applied Geochemistry* **2006**, *21* (3), 515-527. DOI: 10.1016/j.apgeochem.2005.12.004.

(38) Paraquetti, H. H. M.; Ayres, G. A.; de Almeida, M. D.; Molisani, M. M.; Lacerda, L. D. d. Mercury distribution, speciation and flux in the Sepetiba Bay tributaries, SE Brazil. *Water Research* **2004**, *38* (6), 1439-1448. DOI: 10.1016/j.watres.2003.11.039.

(39) Luo Bin, L. B.; Liu Ling, L. L.; Zhang JinLiang , Z. J. Levels and distribution characteristics of heavy metals in sediments in main stream of Huaihe River. *Journal of Environment and Health* **2010**, *27* (12), 1122–1127.

(40) Balcom, P. H.; Hammerschmidt, C. R.; Fitzgerald, W. F.; Lamborg, C. H.; O'Connor, J. S. Seasonal distributions and cycling of mercury and methylmercury in the waters of New York/New Jersey Harbor Estuary. *Marine Chemistry* **2008**, *109* (1-2), 1-17. DOI: 10.1016/j.marchem.2007.09.005.

(41) Coquery, M.; Cossa, D. Mercury speciation in surface waters of the north sea. *Netherlands Journal of Sea Research* **1995**, *34* (4), 245-257. DOI: 10.1016/0077-7579(95)90035-7.

(42) Emmerton, C. A.; Graydon, J. A.; Gareis, J. A. L.; St. Louis, V. L.; Lesack, L. F. W.; Banack, J. K. A.; Hicks, F.; Nafziger, J. Mercury export to the arctic ocean from the Mackenzie River, Canada. *Environmental Science & Technology* **2013**, *47* (14), 7644-7654. DOI: 10.1021/es400715r.

(43) Maurice-Bourgoin, L.; Quemerais, B.; Moreira-Turcq, P.; Seyler, P. Transport, distribution and speciation of

mercury in the Amazon River at the confluence of black and white waters of the Negro and Solimões Rivers. *Hydrological Processes* **2003**, *17* (7), 1405-1417. DOI: 10.1002/hyp.1292.

(44) Sunderland, E. M.; Mason, R. P. Human impacts on open ocean mercury concentrations. *Global Biogeochem Cy* **2007**, *21* (4). DOI: 10.1029/2006gb002876.

(45) Noh, S.; Choi, M.; Kim, E.; Dan, N. P.; Thanh, B. X.; Ha, N. T. V.; Sthiannopkao, S.; Han, S. Influence of salinity intrusion on the speciation and partitioning of mercury in the Mekong River Delta. *Geochimica et Cosmochimica Acta* **2013**, *106*, 379-390. DOI: 10.1016/j.gca.2012.12.018.

(46) Cossa, D.; Coquery, M.; Gobeil, C.; Martin, J. M. Mercury Fluxes at the Ocean Margins. In *Global and Regional Mercury Cycles: Sources, Fluxes and Mass Balances*, 1996; pp 229-247.

(47) Conaway, C. H.; Black, F. J.; Grieb, T. M.; Roy, S.; Flegal, A. R. Mercury in the San Francisco estuary. *Reviews of environmental contamination and toxicology* **2008**, 29-54.

(48) Bergamaschi, B. A.; Fleck, J. A.; Downing, B. D.; Boss, E.; Pellerin, B. A.; Ganju, N. K.; Schoellhamer, D. H.; Byington, A. A.; Heim, W. A.; Stephenson, M.; et al. Mercury Dynamics in a San Francisco Estuary Tidal Wetland: Assessing Dynamics Using In Situ Measurements. *Estuaries and Coasts* **2012**, *35* (4), 1036-1048. DOI: 10.1007/s12237-012-9501-3.

(49) Muresan, B.; Cossa, D.; Coquery, M.; Richard, S. Mercury sources and transformations in a man-perturbed tidal estuary: The Sinnamary Estuary, French Guiana. *Geochimica et Cosmochimica Acta* **2008**, *72* (22), 5416-5430. DOI: 10.1016/j.gca.2008.08.021.

(50) Liu, S.; Zhang, J.; Cui, J. Mercury in four north China estuaries: the Daliaohe, Yalujiang, Luanhe and Dongcunhe. *Journal of Ocean University of Qingdao/Qingdao Haiyang Daxue Xuebao. Qingdao* **2001**, *31* (1), 136-142.

(51) Müller, B.; Berg, M.; Yao, Z. P.; Zhang, X. F.; Wang, D.; Pfluger, A. How polluted is the Yangtze river? Water quality downstream from the Three Gorges Dam. *Science of the total environment* **2008**, *402* (2-3), 232-247.